

Active and Passive Satellite Observations Coupled with Carbon–Nitrogen Synergy for Urban Fossil Fuel CO₂ Emissions Monitoring

Jinchun Yi ^{#,1}, Yiyang Huang ^{#,1}, Ge Han ^{*,1,3}, Hongyuan Zhang ², Zhipeng Pei ², Haotian Luo ¹, Yichi Zhang¹, Tianqi Shi ⁶, Siwei Li ^{1,3}, Wei Gong ^{4,5}

¹Hubei Key Laboratory of Quantitative Remote Sensing of Land and Atmosphere, School of Remote Sensing and Information Engineering, Wuhan University, Wuhan 430079, China.

²State Key Laboratory of Information Engineering in Surveying, Mapping and Remote Sensing, Wuhan University, Luoyu Road No.129, Wuhan 430079, China.

³Perception and Effectiveness Assessment for Carbon-neutrality Efforts, Engineering Research Center of Ministry of Education, Institute for Carbon Neutrality, Wuhan University, Wuhan, China.

⁴Electronic Information School, Wuhan University, Wuhan, China.

⁵Wuhan Institute of Quantum Technology, Wuhan, China.

⁶Laboratoire des Sciences du Climat et de l'Environnement, LSCE/IPSL, CEA-CNRS-UVSQ, Université Paris-Saclay, 91198 Gif-sur-Yvette, France.

Correspondence to: Ge Han (udhan@whu.edu.cn)

These authors contributed equally to this work.

Abstract. Accurate estimation of fossil fuel CO₂ (ffCO₂) emissions is essential for climate prediction and the development of mitigation policies. Top-down carbon – nitrogen joint observations offer the potential for more reliable ffCO₂ estimates. Here, we establish an inversion framework for urban ffCO₂ emissions based on combined active–passive satellite observations. Urban ffCO₂ distributions were first constructed using satellite NO₂ data and CO₂-NO_x emission ratios, and monthly ffCO₂ emissions for selected global cities were then estimated by integrating the total column dry-air carbon dioxide (XCO₂) from the DQ-1 ACDL instrument. Our results show that satellite-derived NO_x emissions provide strong constraints on urban anthropogenic CO₂ estimates. Validation against TCCON ground-based observations indicates that, compared with conventional top-down inversion approaches, our method more accurately reproduces urban ffXCO₂ plume distributions. We further evaluated the influence of different CO₂-NO_x ratio calculation methods on ffCO₂ estimates and found variations exceeding 150, exerting a substantial impact on emission inversions. Under observational constraints, the uncertainty in CO₂-NO_x ratios derived from different methods decreased by 9.79 – 38.78%, and the variation range was reduced by more than 100%, converging toward a consistent magnitude. This study advances understanding of the spatiotemporal patterns of urban ffCO₂ emissions and provides a unified perspective for future CO₂-NO_x-based anthropogenic carbon emission estimation.

1. Introduction

The intensification of global climate change has driven an increasing demand for high-precision monitoring of fossil fuel CO₂ (ffCO₂) emissions (Agency, 2009). The Paris Agreement emphasizes that countries need rapid and timely access to changes in carbon emissions to support policy formulation and implementation. Achieving this goal relies on accurate and verifiable carbon accounting systems. Cities, due to their high concentration of population, energy consumption, and economic activity, contribute over 70% of global anthropogenic CO₂ emissions, making them key units for evaluating emission reduction policies and compliance monitoring (Crippa et al., 2018). Existing global and regional emission inventories primarily adopt bottom-up statistical accounting methods, estimating emissions based on energy production and sector-specific emission factors (Xu et al., 2024; Wei, 2024). However, these inventories often suffer from significant uncertainties due to data delays and incompleteness (Andres et al., 2012; Zhang et al., 2009; Le Quéré et al., 2018).

To overcome the limitations of bottom-up approaches, top-down atmospheric inversion techniques have advanced rapidly in recent years, enabling constraints on regional carbon budgets. Passive satellite remote sensing systems, such as GOSAT and OCO-2/3, can invert XCO₂ over large portions of the globe and have unique potential for identifying local point sources, estimating regional carbon fluxes, and inferring gross primary productivity (Schwandner et al., 2017; Eldering et al., 2017; Köhler et al., 2018; Han et al., 2018; Sun et al., 2018b). Nonetheless, top-down inversion methods also rely on accurate prior emission estimates. Inventories that downscale national or regional emissions to high spatial and temporal resolution often suffer from incomplete socio-economic data and inaccurate emission conversion factors, leading to substantial uncertainties in urban emission estimates (Gately and Hutyra, 2017). Moreover, conventional top-down CO₂ inversion studies have focused primarily on quantifying terrestrial ecosystem carbon fluxes, typically assuming fossil fuel emissions are known and unbiased. This complicates direct inference of anthropogenic emissions from CO₂ observations due to the atmospheric mixing of fossil fuel and ecosystem fluxes (Ye et al., 2020).

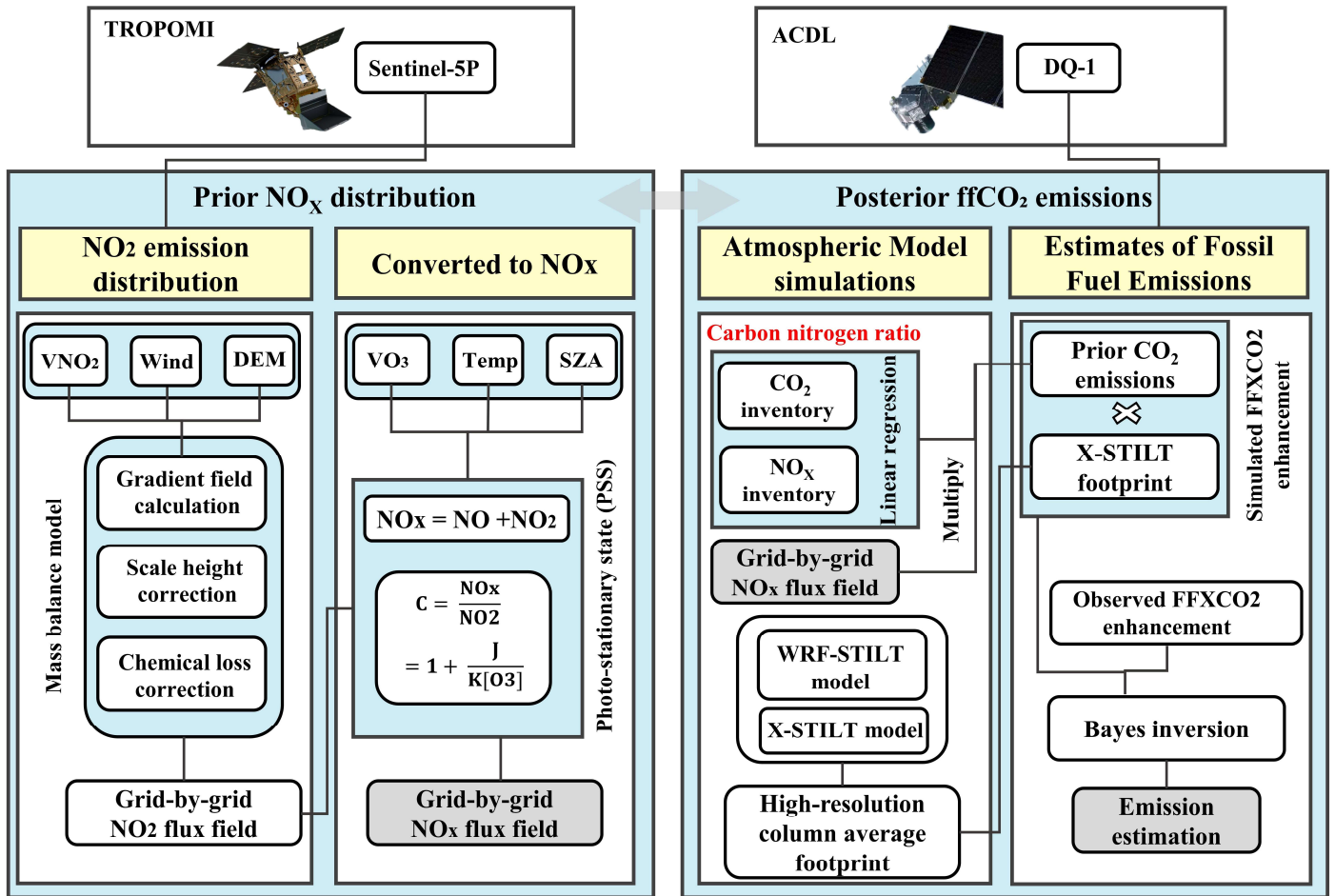
Coupled carbon-nitrogen observations offer a new perspective to address this gap (Reuter et al., 2019; Yang et al., 2023). Nitrogen oxides (NO_x = NO + NO₂) are major co-emitted species from fossil fuel combustion, with emission intensity and spatial distribution closely correlated with ffCO₂ (Feng et al., 2024). Studies have shown that in regions with varying pollution levels, XCO₂ anomalies spatially correlate with tropospheric NO₂ column densities (Hakkarainen et al., 2016). Moreover, the CO₂-to-NO_x ratio is often more stable than individual emission amounts because systematic biases in fossil fuel consumption affect both CO₂ and NO_x statistics (Konovalov et al., 2016). Recent research suggests that optimized NO_x emissions, combined with CO₂-to-NO_x ratios from bottom-up inventories, can provide more accurate ffCO₂ estimates (Zheng et al., 2020). For instance, Zheng et al. used TROPOMI NO₂ data to estimate 10-day moving averages of Chinese ffCO₂ emissions during the COVID-19 pandemic, finding an 11.5% decline compared to the same period in 2019 (Zheng et al., 2020). Liu et al. validated the feasibility of NO_x-based ffCO₂ estimation by comparing inferred CO₂ emissions with highly accurate stack measurements from eight large US power plants (Liu et al., 2020).

60 High-resolution NO₂ column observations, such as those from Sentinel-5P/TROPOMI, can be inverted using a mass-balance
61 framework to derive accurate NO_x gridded fluxes(Beirle et al., 2023; Qin et al., 2023; Sun, 2022; Sun et al., 2021). These NO_x fluxes
62 can inform the prior spatial allocation of CO₂ emissions due to the co-emission consistency of fossil fuel sources, and the high
63 temporal resolution of TROPOMI allows rapid updates of CO₂ priors, mitigating the lag inherent in static inventories(Zhang et al.,
64 2022).

65 The CO₂-to-NO_x ratio is crucial for converting NO_x emissions into ffCO₂ estimates. However, because the CO₂-to-NO_x ratio
66 used in this study is calculated from CO₂ emissions and NO_x emissions, there is currently a lack of accurate top-down measurement
67 methods, most studies derive this ratio from inventories, and different calculation methods yield significantly different values.
68 Assimilating observational data to invert CO₂-to-NO_x ratios is therefore key to reducing uncertainties in ffCO₂ estimation. Passive
69 top-down observations are limited by cloud cover, aerosols, and solar irradiance, and in complex multi-source and topographic
70 environments, signal attribution is challenging, restricting the accuracy and stability of city-scale inversions(Miller et al., 2014).

71 In 2022, China launched DQ-1, the world's first CO₂ lidar satellite, equipped with an IPDA lidar (ACDL) capable of high
72 signal-to-noise ratio, day-and-night, all-weather observations. The dual-wavelength differential method mitigates interference from
73 aerosols and thin clouds(Han et al., 2017; Han et al., 2025). Compared to passive satellites, IPDA lidar offers unique advantages in
74 urban plume detection and fine-scale emission inversion(Kiemle et al., 2017; Kiemle et al., 2011; Yi et al., 2024). Previous studies
75 using DQ-1 XCO₂ data successfully constrained point-source emissions(Cheng et al., 2025; Han et al., 2024; Zhang et al., 2025),
76 and Yi et al. developed a kilometer-scale urban flux inversion system based on ACDL measurements, comparing its constraints to
77 passive systems like OCO-2/3(Yi et al., 2025).

78 In this study, we propose a city-scale ffCO₂ inversion framework that jointly assimilates active and passive satellite observations,
79 dynamically bridging NO_x and CO₂ emissions via the CO₂-to-NO_x ratio. The workflow is illustrated in Fig. 1. TROPOMI NO₂
80 column data are first used to invert NO_x gridded emissions via a mass-balance approach. Combined with prior CO₂-to-NO_x ratios,
81 these NO_x fluxes are converted into CO₂ priors. DQ-1 XCO₂-Lidar along-track measurements are then assimilated using WRF-
82 STILT high-resolution atmospheric transport simulations within a Bayesian inversion framework to estimate total city emissions
83 and explicitly quantify observational and transport uncertainties. We applied this approach to Beijing, Paris, and Cairo, representing
84 cities with diverse topographies and emission patterns, using August 2022 TROPOMI and DQ-1/ACDL data to evaluate the
85 framework's ability to provide robust, high-resolution urban emission estimates. It is noteworthy that no unified CO₂-to-NO_x ratio
86 calculation method currently exists, and different methods yield divergent values, which can significantly bias final emission
87 estimates. This study systematically evaluates the influence of prior CO₂-to-NO_x ratio calculation methods on inversion outcomes,
88 demonstrating that Bayesian assimilation can substantially reduce this uncertainty, converging different ratios to a consistent
89 magnitude. This framework offers a unified approach for estimating urban emissions under limited or uncertain inventory conditions,
90 providing a timely and reliable method for reporting anthropogenic CO₂ emissions at the city scale.



91
92 **Figure 1 Technical framework diagram**

93 The remainder of this paper is structured as follows. Section 2 introduces the datasets and methods used in this study. Section
94 3 presents the results of NO_x emission estimation in Paris, Cairo, and Beijing based on TROPOMI observations combined with a
95 mass-balance approach, followed by city-scale ffCO₂ inversion results obtained by assimilating DQ-1 ACDL observations within a
96 Bayesian framework. Section 4 examines the influence of different prior CO₂-to-NO_x ratio calculation methods on the inversion
97 process and highlights the importance of optimizing the CO₂-to-NO_x ratio using observational data. Finally, Section 5 summarizes
98 and discusses the potential of the multi-source satellite Bayesian inversion framework for constraining urban CO₂ emissions, and
99 emphasizes the significance of optimized CO₂-to-NO_x ratios for improving the accuracy of urban ffCO₂ estimates.

100 **2. Materials and methods**

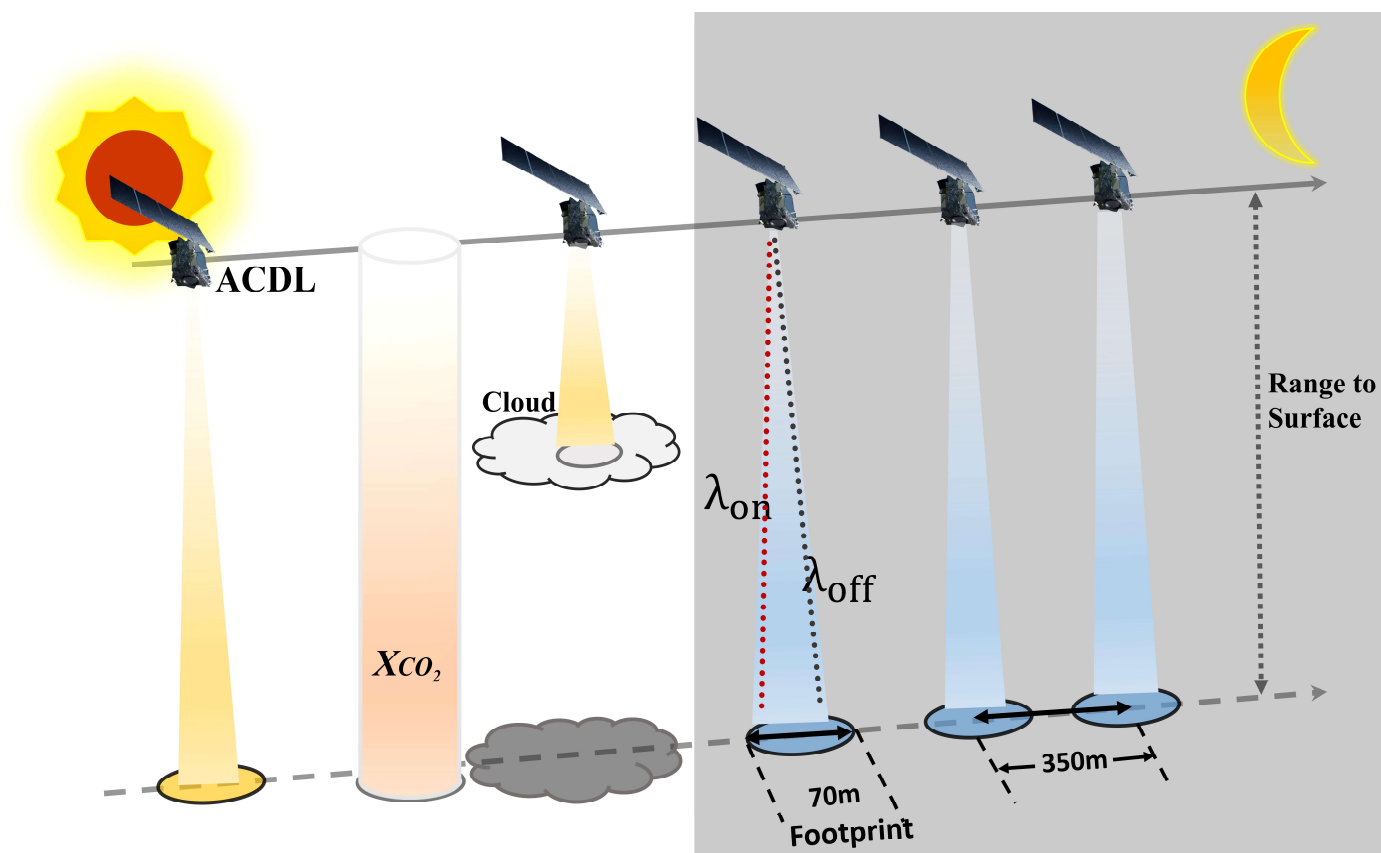
101 **2.1. Data**

102 **2.1.1. ACDL Productions**

103 The concept of DQ-1 was first proposed in 2012 with the aim of developing a satellite-borne lidar system analogous to the
104 Cloud-Aerosol Lidar with Orthogonal Polarization (CALIOP) onboard CALIPSO, and it was officially approved as a national

105 project in 2017. Unlike conventional environmental monitoring satellites, DQ-1 is distinguished by its breakthrough active remote
106 sensing payload—the Atmospheric Carbon Dioxide Differential Absorption Lidar (ACDL)—which enables active “top-down”
107 observations of atmospheric CO₂. The ACDL underwent successive stages of laboratory prototype development and airborne
108 validation before its successful launch onboard the DQ-1 satellite into a near-polar sun-synchronous orbit at an altitude of ~705 km
109 on April 18, 2022. Operational observations commenced in late May of the same year. This study primarily analyzes data collected
110 August 2022.

111 The ACDL operates on the principle of Integrated Path Differential Absorption (IPDA) lidar, retrieving atmospheric column-
112 averaged CO₂ concentrations (XCO₂) via differential absorption techniques. The inversion methodology and data product
113 specifications have been described in detail elsewhere; here, we provide only a brief overview (Han et al., 2025). The instrument
114 transmits two nearly simultaneous laser pulses: one at a strong absorption line of CO₂ (R16, referred to as the “online” wavelength)
115 and the other at a nearby weak absorption line (the “offline” wavelength). These are stabilized at 6361.225 cm⁻¹ and 6360.981 cm⁻¹,
116 corresponding to 1572.024 nm and 1572.085 nm, respectively. By comparing the differential attenuation between the online and
117 offline signals, the system effectively mitigates the influence of aerosols and other interfering species, except water vapor, thereby
118 enabling accurate retrievals of XCO₂. The inversion process relies on dedicated algorithms, with the central concept being that the
119 small wavelength offset produces differential absorption, which enhances the sensitivity of CO₂ detection (details of the ACDL
120 XCO₂ retrieval algorithm are provided in the Appendix A1).



121
122 **Figure 2 the schematic diagram for DQ-1's detection principle**

123
124 Figure 2 illustrates the schematic of the DQ-1 measurement principle. The XCO₂ products generated by ACDL are provided in
125 a point-sampling mode analogous to that of GOSAT. The lidar records one footprint of approximately 70 m every ~350 m along the
126 satellite ground track. Additional details of the ACDL operating parameters are provided in the Appendix A1.

127 **2.1.2. TROPOMI Productions**

128 TROPOMI is a nadir-viewing spectrometer onboard ESA's Sentinel-5 Precursor (S5P) satellite, which was launched in October
129 2017. Operating in an ascending Sun-synchronous polar orbit with an equator crossing time of approximately 13:30 local time,
130 TROPOMI measures a range of trace gases as well as cloud and aerosol properties across four spectral channels (ultraviolet, visible,
131 near-infrared, and shortwave infrared). The instrument's minimum pixel size was about 3.5×7 km² at nadir before being reduced
132 to $\sim 3.5 \times 5.5$ km² on 6 August 2019 (Veefkind et al., 2012). In this study, we used the S5P-PAL dataset (consistent with version
133 2.3.1) (Eskes et al., 2021) covering the period from 1 August to 1 September 2022, obtained from <https://data-portal.s5p-pal.com>

134 To ensure data quality, we filtered out pixels with a `qa_value` < 0.75 (Qin et al., 2023), and, following van Geffen et al., removed
135 cloudy pixels (cloud radiance fraction > 50%) as well as anomalies (e.g., eclipses) from the TROPOMI NO₂ dataset (Van Geffen et
136 al., 2022). To test our algorithm framework on a robust dataset, we selected summer NO₂ observations for three cities located in the
137 mid-latitudes of the Northern Hemisphere, avoiding winter measurements that may be complicated by potential snow cover.
138 Furthermore, given the need for city-scale accuracy, air mass factor (AMF) corrections were applied locally following the method
139 described in (Beirle et al., 2023).

140 Sun et al. proposed an oversampling algorithm to project multi-satellite, multi-species observations onto a common grid, with
141 code publicly available on GitHub (https://github.com/Kang-Sun-CfA/Oversampling_matlab/) (Sun et al., 2018a). In this work, we
142 applied this algorithm to the pre-processed TROPOMI overpass data, generating oversampled grids at 1 km resolution following
143 the procedure described in (Sun, 2022).

144 **2.1.3. Meteorological and DEM data**

145 For the estimation of CO₂ emissions through model simulations, we utilized meteorological parameters from the National
146 Centers for Environmental Prediction Final (NCEP FNL) operational global analysis dataset (National Centers for Environmental
147 Prediction/National Weather Service/NOAA/U.S. Department of Commerce, 2015). The ds083.3 dataset is provided on a $0.25^\circ \times$
148 0.25° latitude–longitude grid and updated every six hours via the Global Data Assimilation System (GDAS)
149 (<https://rda.ucar.edu/datasets/ds083-3/>). It covers 32 vertical levels, ranging from the surface to the top of the atmosphere, including
150 the ground level and 31 isobaric layers from 1000 hPa to 1 hPa. Essential variables such as surface pressure, geopotential height,
151 temperature, relative humidity, and zonal and meridional wind components were used as the main meteorological inputs for driving

152 the WRF-STILT simulations.

153 The wind vector data were obtained from the ERA5 reanalysis dataset (<https://doi.org/10.24381/cds.adbb2d47>)(Hersbach et
154 al., 2023). We extracted hourly 10 m and 100 m wind vectors at 0.25° spatial resolution for the three selected cities during the period
155 from 1 August to 1 September 2022. The 10 m wind vectors are used to approximate near-surface winds, whereas the 100 m wind
156 vectors represent horizontal transport within the planetary boundary layer. These data were averaged to daily values and
157 subsequently interpolated to match the grid resolution of the column concentration fields described in Section 2.3.1.

158 Digital elevation data were obtained from the GMTED2010 dataset (<https://www.usgs.gov/coastal-changes-and-impacts/gmted2010>)(Danielson and Gesch, 2011). The DEM was resampled and mapped to the same spatial grid as the
159 concentration and wind fields to ensure consistency across all datasets.
160

161 **2.1.4. Emissions Inventory**

162 In this study, multiple emission inventories were used to estimate fossil fuel CO₂ (ffCO₂) emissions and to calculate the CO₂-
163 to-NO_x ratio. In the urban observation system simulation experiment (Section 3), the GEMS inventory (0.1° resolution) for NO_x and
164 CO₂ emissions(Wang et al., 2013; Huang et al., 2017) was used to derive the prior CO₂-to-NO_x ratio (available at:
165 <https://gems.sustech.edu.cn/data>). For comparison, we also employed the gridded fossil fuel CO₂ emissions inventory from the
166 Open - source Data Inventory for Atmospheric Carbon dioxide (ODIAC, Version 2024, 1 km resolution;
167 <https://db.cger.nies.go.jp/dataset/ODIAC/>)(Oda and Maksyutov, 2015). In Section 4, we further utilized the sectoral and 0.1° gridded
168 NO_x and CO₂ inventories from the Emissions Database for Global Atmospheric Research (EDGAR;
169 https://edgar.jrc.ec.europa.eu/emissions_data_and_maps)(Crippa et al., 2018), as well as the sectoral NO_x and CO₂ inventories from
170 the Multi-resolution Emission Inventory model for Climate and air pollution research (MEIC; <http://meicmodel.org.cn/>)(Team,
171 2012). Using different approaches to calculate the CO₂-to-NO_x ratio, we quantified the variations arising from different inventory
172 inputs and assessed their impact on emission inversions.

173 **2.2. Methodology**

174 **2.2.1. Calculation of Prior Distribution for CO₂ Emissions**

175 **(1) Mass Balance Method**

176 In previous studies, numerous works have detailed the theoretical derivation for inferring gridded fluxes from column
177 observations(Beirle et al., 2023; Huang et al., 2024; Koene et al., 2024; Qin et al., 2023; Rey-Pommier et al., 2025; Sun, 2022;
178 Ayazpour et al., 2025). Such frameworks are generally based on solutions to the atmospheric continuity equation. Divergence-based
179 approaches typically rely on several key assumptions: (1) exchanges above the planetary boundary layer (column top) and at the

surface (column bottom) are neglected, effectively assuming two-dimensional diffusion; (2) horizontal turbulent transport is ignored at coarse grid resolutions; and (3) the deposition term S is treated using a first-order chemical approximation. Starting from the unsteady, source-driven atmospheric continuity equation, the gridded flux of a given species, such as NO_2 , can be derived from satellite column observations, with the resulting flux $\langle E_{\text{NO}_2} \rangle$ expressed as in Equation 1.

$$\langle E_{\text{NO}_2} \rangle = \langle \vec{u} \cdot (\nabla V_{\text{NO}_2}) \rangle + \frac{\langle V_{\text{NO}} \vec{u}_{10} \cdot (\nabla z_0) \rangle}{H} + \frac{\langle V_{\text{NO}_2} \rangle}{\tau} \quad (1)$$

The detailed derivation is provided in Appendix A2. To fully exploit the available data while accounting for observational errors, spatial gradients were computed along the zonal, meridional, and both diagonal directions. Gradients were numerically approximated using second-order central differences, multiplied by the corresponding decomposed wind vectors, and then averaged. For boundary grid points, one-sided differences were applied.

(2) Convert NO_2 to NO_x

Nitrogen oxides ($\text{NO}_x = \text{NO} + \text{NO}_2$) do not exist independently in the troposphere, as NO and NO_2 continuously interconvert, while the total NO_x remains relatively stable. To convert between NO_2 column densities and total NO_x columns, Sun et al. applied a fixed coefficient of 1.32. In this study, we adopt a more rigorous approach to derive the conversion factor, as expressed in Equation 2 (Beirle et al., 2023), based on the photostationary steady-state assumption:

$$\begin{cases} V_{\text{NO}_x} = \alpha V_{\text{NO}} = \left(1 + \frac{J}{K X_{\text{O}_3}}\right) V_{\text{NO}_2} \\ J = k_1 * \exp\left(-\frac{k_2}{\cos(\text{SZA})}\right) \\ K = k_3 * \exp\left(-\frac{k_4}{T}\right) \end{cases} \quad (2)$$

Here, J represents the photolysis frequency of NO_2 , calculated following the methodology in (Dickerson et al., 1982). The rate constants k_1 and k_2 are set to 0.0167 and 0.575, respectively. The solar zenith angle (SZA) can be directly determined from the local latitude, longitude, and time; in this study, SZA values are obtained from the TROPOMI satellite metadata. K denotes the chemical reaction rate constants for NO with O_3 , expressed in $\text{cm}^3/(\text{mol} \cdot \text{s})$ and recommended by IUPAC, with $k_3=2.07 \cdot 10^{-12}$ and $k_4=1400$. The ozone mixing ratio, X_{O_3} , is derived from the ESCiMo project (Brenninkmeijer and Cai, 2016), and T represents the boundary-layer mean temperature obtained from ERA5 reanalysis data. Under these definitions, Equation 2 can be rewritten as:

$$X = \alpha * \langle E_{\text{NO}_2} \rangle \quad (3)$$

Using Equation 3 we can obtain grid-resolved estimates of NO_x fluxes, which serve as the prior distribution for fossil fuel CO_2 (ffCO_2) emissions. These estimates provide a data-driven prior inventory for subsequent steps in the inversion framework.

204 (3) Scale height and Chemical lifetime

205 Regarding the selection of scale height and first-order chemical lifetime, previous studies, such as Beirle et al., employed fixed
206 empirical scale height values and adjusted terrain correction terms to obtain optimal estimates(Beirle et al., 2023). Their chemical
207 lifetime was calculated using a compensation method that accounted for losses integrated over residence times within a 15 km buffer.
208 While effective at point-source scales, this approach is not directly applicable to our study. In the present work, we follow Sun et
209 al.'s purely data-driven approach, which leverages observational data without introducing additional assumptions, constructing a
210 linear regression model to determine these parameters(Sun, 2022). This observation-driven fitting method not only reduces errors
211 arising from new assumptions but also mitigates biases caused by grid resampling and near-surface wind selection.

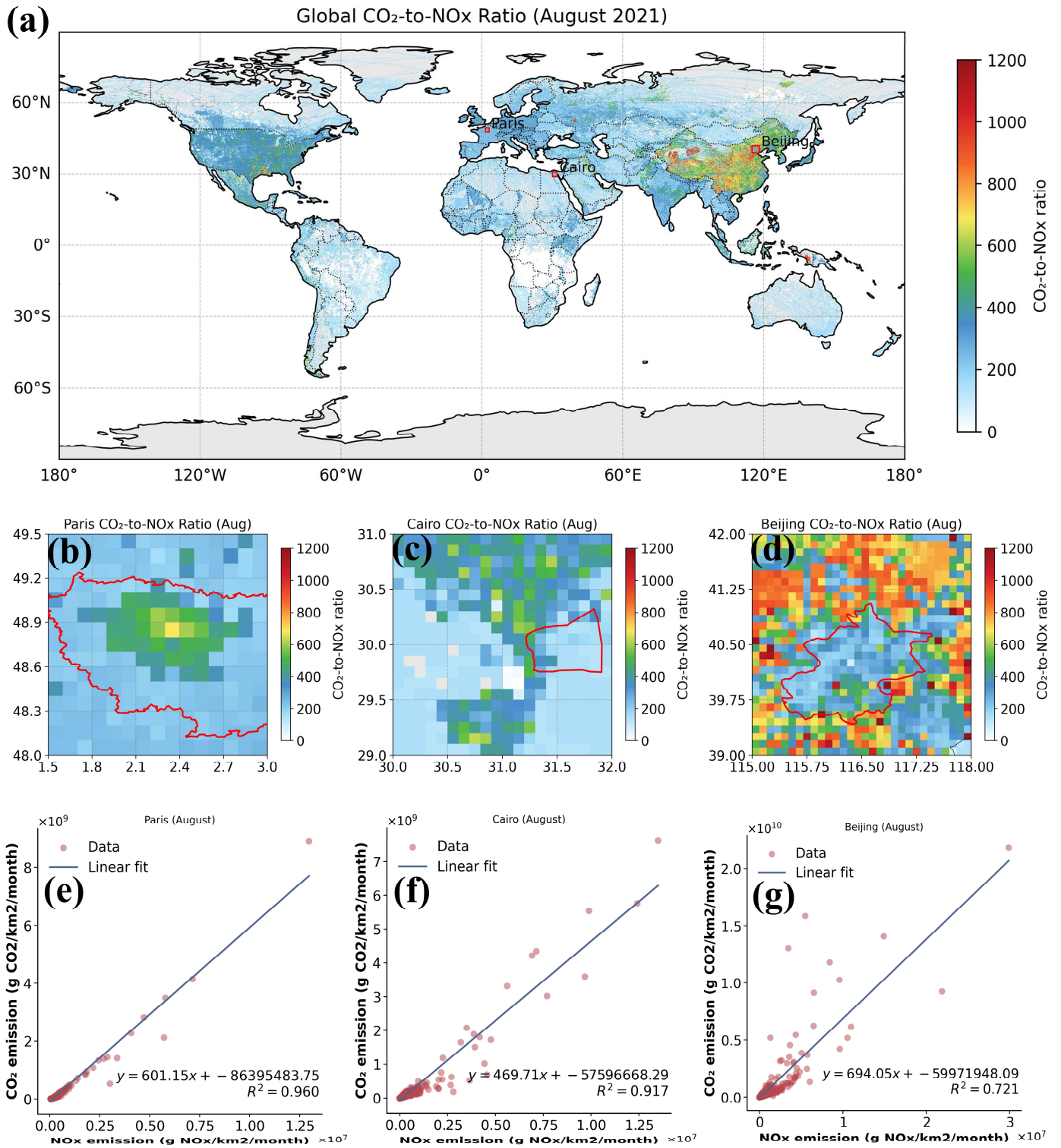
212 To suppress excessive noise in single-day fits, we perform monthly regressions and adopt the temporal and spatial mean over
213 the month as the final estimate, representing an aggregate over the full spatial domain, the entire month, and the troposphere. The
214 retrieved scale height and first-order chemical lifetime are then applied back into Equations 4 and 6 to obtain the final gridded NO_x
215 vertical fluxes.

216 After terrain correction, the gridded flux fields remove a substantial portion of strong emission signals obscured by wind
217 divergence and negative divergence artifacts, while the chemical correction term adjusts residual minor negative biases(Sun, 2022;
218 Sun et al., 2018a; Beirle et al., 2023). Any remaining small negative values after these corrections are set to zero.

219 (4) Calculation of Prior CO_2 -to- NO_x Ratio

220 We used the prior CO_2 -to- NO_x ratio in combination with TROPOMI-derived NO_x emission distributions to obtain an initial
221 characterization of urban prior ffCO_2 emissions. Following the approach of Feng et al., who calculated the CO_2 -to- NO_x ratio by
222 dividing gridded CO_2 and NO_x emission inventories(Feng et al., 2024), we derived city-specific prior CO_2 -to- NO_x ratio using the
223 0.1° CO_2 and NO_x inventories from GEMS (<https://gems.sustech.edu.cn/data/database>). Unlike Feng et al., who focused on grid-
224 level CO_2 -to- NO_x ratio, we fitted the gridded ratios across each study region to obtain an integrated city-level CO_2 -to- NO_x ratio,
225 which is more suitable for subsequent inversion analyses (Fig. 3). Details on the associated uncertainties are provided in Section
226 4.1.

227 Figure 3 illustrates our method for calculating the prior CO_2 -to- NO_x ratio. By fitting the 0.1° gridded ratios for each city, we
228 obtained overall city-scale values. The coefficients of determination (R^2) for Paris, Cairo, and Beijing were 0.96, 0.917, and 0.76,
229 respectively.



231
 232 **Figure 3** Schematic diagram of prior CO₂-to-NO_x ratio calculation methods. Panel (a) shows the global gridded CO₂-to-NO_x ratio derived
 233 from GMES data. Panels (b)–(d) present the gridded CO₂-to-NO_x ratio for Paris, Cairo, and Beijing (the red lines indicate the boundaries
 234 of each city). Panels (e)–(g) display the overall CO₂-to-NO_x ratio fitting results for the three cities. We used the Île-de-France administrative
 235 boundary to depict Paris in the figures, rather than the city proper. Although our actual study area only covers a subset of Île-de-France
 236 (1.5–3° E, 48–49.5° N)

237 Recently, an increasing number of studies have employed NO_x emissions to estimate ffCO₂ emissions(Feng et al., 2024; Zheng
 238 et al., 2020; Xu et al., 2025; Yang et al., 2023; Berezin et al., 2013; Zhang et al., 2022). In inversion methods based on NO_x emissions,

239 the choice of the prior CO₂-to-NO_x ratio directly affects the emission estimates. Uncertainty in the prior ratio propagates to the
240 estimated ffCO₂ emissions, influencing both their magnitude and spatial distribution. To evaluate this effect, we selected several
241 widely used CO₂-to-NO_x ratio calculation methods and systematically assessed their associated uncertainties (results see Section
242 4.1 and Appendix A6).

- 243 - M.1 Grid-level CO₂-to-NO_x ratio derived directly from gridded CO₂ and NO_x inventories(Feng et al., 2024). Since this study
244 scales emissions to the city level, we further fitted the grid-level ratios to obtain city-integrated CO₂-to-NO_x ratios. M.1
245 calculations were based on the GEMS gridded inventory.
- 246 - M.2 CO₂-to-NO_x ratios calculated using sectoral emission factors for CO₂ and NO_x(Zheng et al., 2020). We derived city-scale
247 ratios by aggregating across all sectors. M.2 used the GEMS sectoral inventory.
- 248 - M.3 CO₂-to-NO_x ratios derived from near-real-time satellite observations. Background-stable NO_x plumes were used to
249 constrain CO₂ plumes, and joint fitting of the two concentrations was performed using the cross-sectional flux method(Xu et
250 al., 2025; Reuter et al., 2019). The CO₂-to-NO_x ratio was obtained directly from the half-width at half-maximum. Following
251 this approach, we used TROPOMI and OCO-2 observations to calculate city-scale ratios.
- 252 - M.4 Same as M.2, but the MEIC sectoral inventory was used for Beijing.
- 253 - M.5 Same as M.1, but calculations were based on the EDGAR gridded inventory.
- 254 - M.6 Same as M.2, but calculations were based on the EDGAR sectoral inventory.

255 2.2.2. Estimating ffCO₂ emissions by WRF-STILT simulations

256 (1) Quantifying ffXCO₂ enhancements

257 Distinguishing anthropogenic emission signals from the surrounding “clean” background in XCO₂ observations is a central
258 challenge for constraining urban carbon emissions via satellite. Definitions of “background” vary across studies. In this work, we
259 define the background as atmospheric XCO₂ that is unaffected by local emissions within the study region. Following the approach
260 proposed by (Ye et al., 2020)in constraining urban emissions using OCO-2 observations, we adopt a baseline calculation strategy
261 that incorporates latitudinal gradients.

262 In this framework, XCO₂ is decomposed into two components: $XCO2_{trend}$, representing the regional-scale, non-local trend,
263 and $XCO2_{local}$, whose standard deviation σ_{local} characterizes local-scale variability. Samples satisfying $XCO2 < XCO2_{trend} +$
264 $0.5\sigma_{local}$ are selected as “background samples,” as they exhibit lower local spatial variability compared with data influenced by
265 fossil fuel emissions. These background samples are then subjected to linear regression to derive the background baseline and
266 characterize its spatial variation.

267 (2) X-Stochastic Time-Inverted Lagrangian Transport model for ACDL productions

268 We employ the X-STILT V1 model to trace CO₂ concentration variations driven by prior emission information. X-STILT
 269 integrates satellite profile data and enables a comprehensive uncertainty assessment of urban XCO₂ enhancements on a per-
 270 observation basis (Wu et al., 2018). Originally developed to extract urban signals from passive OCO-2 XCO₂ observations, we have
 271 adapted the framework for use with the active CO₂ satellite DQ-1, with appropriate modifications. The relationship between
 272 XCO₂^{Lidar} (DQ-1 XCO₂ observations) measurements and the CO₂ vertical profile, CO₂(p), can be formulated as follows:

$$273 \quad XCO_2^{Lidar} = \frac{\int_{p_{surface}}^{p_{toa}} CO_2(p) WF(p) dp}{\int_{p_{surface}}^{p_{toa}} WF(p) dp} = \sum_{n=1}^{toa} \frac{WF(p_n)}{IWF} \cdot CO_2(p_n) \quad (4)$$

274 Here, p_{toa} represents the pressure at the bottom height of the ACDL, and $p_{surface}$ represents the pressure corresponding
 275 to the surface elevation at the laser footprint. WF and IWF denote the weighting function and the normalized weighting function
 276 of the ACDL, respectively. A detailed description is provided in Appendix A1.

277 We approximate the CO₂ concentration by summing the background concentration with the simulated ffCO₂ enhancement.
 278 Here, the simulated ffCO₂ enhancement, $\Delta CO_2_{ffCO_2}(p) = \langle ffCO_2, foot(p) \rangle$, is obtained by interpolating the modeled ffCO₂
 279 fluxes along tracer-tagged footprints. Consequently, the relationship between the ffCO₂ fluxes and the simulated $XCO_2^{Lidar}_{mod}$, is
 280 established, yielding the modeled fossil fuel CO₂ enhancement $XCO_2^{Lidar}_{ffCO_2, mod}$ along the lidar track:

$$281 \quad XCO_2^{Lidar}_{ffCO_2, mod} = XCO_2^{Lidar}_{mod} - XCO_2^{Lidar}_{background} = \sum_{n=1}^{toa} \frac{WF(p_n)}{IWF} \cdot \langle emissions, foot(p_n) \rangle \quad (5)$$

282 $XCO_2^{Lidar}_{background}$ represents the background concentration along the selected DQ-1 orbit (see Section 2.2.2 (1)). The operator
 283 \langle, \rangle denotes an inner product, $emissions$ is the prior emission flux, and $foot(p_n)$ represents the modeled footprint at different
 284 vertical layers. Using the above formulation, the mathematical foundation for the inversion is established. By integrating footprints
 285 across multiple release heights, the equation can be further simplified. In this study, we define the ffXCO₂ enhancement simulated
 286 via the atmospheric transport model as:

$$287 \quad XSTILT^{Lidar} = \sum_{n=1}^{toa} \frac{WF(p_n)}{IWF} \cdot foot(h_n) \quad (6)$$

$$288 \quad XCO_2^{Lidar}_{ffCO_2, mod} = \langle XSTILT^{Lidar}, emissions \rangle \quad (7)$$

289 Here, $XSTILT^{Lidar}$ is defined as the column-averaged footprint, corresponding to the column-averaged CO₂ concentration.
 290 The inner product of the column-averaged footprint and the prior emission flux yields the simulated XCO₂ enhancement.

291 (3) Bayes inversion

292 We used the NO_x emissions obtained previously as prior fluxes and, through the CO₂-to-NO_x ratio, established the relationship

between the prior emissions and the XCO₂ observed by DQ-1 (Equation 9). The XCO₂ enhancements estimated from DQ-1 observations were then employed to impose “top-down” constraints on the simulated results. Following the approaches of (Che et al., 2024; Ye et al., 2020; Wang et al., 2014; Sheng et al., 2025), we applied a Bayesian inversion framework to optimize the prior emission estimates.

$$y_{obs} = y_{sim} \cdot \lambda + \varepsilon_p \quad (8)$$

Here, y_{obs} and y_{sim} represent the observed ffXCO₂ enhancements and the simulated NO_x enhancements, respectively. The symbol λ denotes the CO₂-to-NO_x ratio, and ε_p represents the observational error, which encompasses contributions from DQ-1 measurement uncertainties, model errors, and errors in model parameters. It is defined as follows:

$$\begin{cases} y_{obs} = \int_{latitude1}^{latitude2} ffXCO2_{obs} dt \\ y_{sim} = \int_{latitude1}^{latitude2} \langle X, footprint \rangle dt \end{cases} \quad (9)$$

$$\varepsilon_{obs} = \sqrt{\sigma_{measurement}^2 + \sigma_{sim}^2} \quad (10)$$

In this context, ffXCO₂_{obs} represents the DQ-1 XCO₂ enhancement after background concentration removal. The notation $\langle X, footprint \rangle$ denotes the simulated NO_x enhancement, obtained by convolving the NO_x emission inventory X with the STILT-derived footprint (It should be noted that the footprints used here represent hourly footprints during the simulation period, whereas the NO_x emissions are monthly emissions derived using the method described in Section 2.2.1. Therefore, we use the New High Resolution Temporal Profiles in EDGAR dataset (https://edgar.jrc.ec.europa.eu/dataset_temp_profile) to distribute the monthly NO_x emissions to each hourly footprint). Pseudo-observations, ffXCO₂_{obs}, are generated by averaging DQ-1 measurements over one-second intervals along the satellite track (~7 km), together with the corresponding simulated values.

Following the Bayesian inversion approach, the state vector λ is expressed in terms of the CO₂-to-NO_x ratio, representing the relationship between urban fossil fuel CO₂ and NO_x emissions. The Jacobian matrix is derived from the simulated NO_x enhancement y_{sim} . Here, $\sigma_{measurement}^2$ represents the observational error variance, and σ_{sim}^2 denotes the model transport error variance. DQ-1 observations are assumed unbiased with respect to the true state. To account for measurement uncertainty, random Gaussian noise with a standard deviation of 0.3 ppm—representing the lower limit of observational error—is added to the observations.

By minimizing the loss function, we obtain the posterior CO₂-to-NO_x ratio $\hat{\lambda}$ and posterior uncertainty $\hat{\sigma}$:

$$\hat{\lambda} = \lambda + \sigma_{sim}^2 y_{sim}^T (y_{sim} S_{obs} y_{sim}^T + S_{obs})^{-1} (y_{obs} - y_{sim} \lambda) \quad (11)$$

$$\hat{\sigma}^2 = (y_{sim}^T S_{obs}^{-1} y_{sim} + \sigma_{sim}^{-2})^{-1} \quad (12)$$

Here, S_{obs} is a diagonal matrix, with the diagonal entries representing the observational error variances ε_{obs}^2 for each orbit.

319 the prior uncertainty σ_{sim} is primarily derived from the uncertainties in the prior NO_x emission distribution σ_{NOx} and the prior
320 CO₂-to-NO_x ratio $\sigma_{C/N}$ as equation 13:

$$321 \quad \sigma_{sim} = \sqrt{\sigma_{NOx}^2 + \sigma_{C/N}^2} \quad (13)$$

322 3. Urban Observation System Simulation Experiment

323 3.1. Satellite-driven urban NO_x emission distribution

324 As described in Section 2.2.1, we applied the mass balance approach in the three cities to derive prior NO_x gridded inventories,
325 which serve as the basis for constructing ffCO₂ gridded emissions. The grid resolution was set to 5 km × 5 km. Figure 4 illustrates
326 the detailed NO_x fluxes for August 2022 over Beijing, Paris, and Cairo, produced entirely via a top-down approach, with panels (a)–
327 (c) corresponding to Beijing, Paris, and Cairo, respectively.

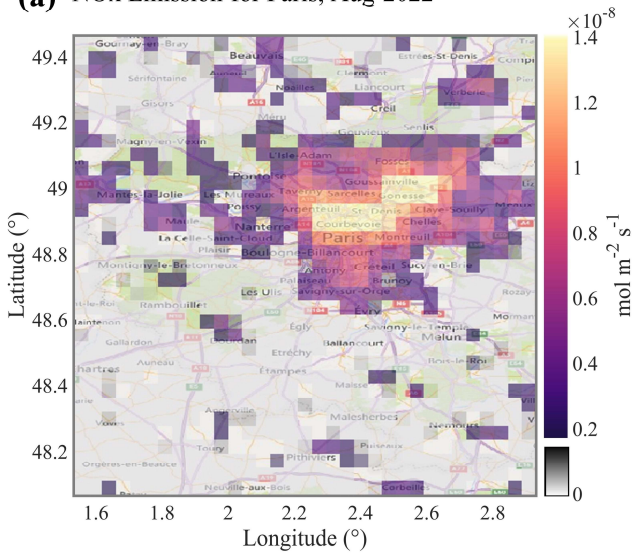
328 From the figure, it is evident that the average NO_x flux magnitude in all three cities is on the order of $\sim 10^{-8}$ mol m⁻² s⁻¹. However,
329 their spatial distributions differ considerably. Both Paris and Cairo exhibit highly concentrated emission patterns. In Cairo, the
330 central urban area and industrial zones display peak NO_x fluxes on the order of $\sim 10^{-7}$ mol m⁻² s⁻¹. These high-flux regions sharply
331 decrease with distance from the center, highlighting a pronounced urban boundary effect. In contrast, Beijing not only exhibits
332 strong emissions in the central urban area (within the Sixth Ring Road) but also features numerous dispersed point- and area-like
333 sources in suburban districts (e.g., Fangshan in the southwest) and in the surrounding hills and mountains. Compared with Cairo’s
334 concentrated emissions, Beijing’s peak NO_x grid flux in the urban core is nearly one order of magnitude lower (see the color scale
335 mapping in Fig. 4); however, due to the city’s larger spatial extent, the total flux remains substantially higher than that of Cairo.

336 Beijing’s topography, with higher elevations in the northwest and lower elevations in the southeast, can induce local wind
337 divergence over hilly and mountainous areas. This effect may generate false positives when using the divergence method (Sun et al.,
338 2021; Liu et al., 2021). In the northwestern suburban mountains of Beijing, the mean wind divergence can reach magnitudes of \sim
339 $\pm 10^{-4}$ s⁻¹, while TROPOMI NO₂ column densities are on the order of 10^{-4} mol m⁻². Such magnitudes are comparable to mid-scale
340 urban averages or point-source emissions. Neglecting the divergence term can result in genuine emissions being omitted, while
341 background fluxes induced by terrain or wind divergence are mistakenly included. Following (Sun, 2022), we applied Eq. A5 to
342 reconstruct the wind-divergence term using surface wind and terrain gradients, thereby reintegrating previously neglected area-like
343 emissions. Using Beirle et al.’s methodology, we integrated the net gridded fluxes within a 60 km radius centered on Beijing over
344 the entire year of 2022 to estimate the city’s annual NO_x emissions at 251,450 t. This value is approximately 9.7% higher than the
345 2022 annual emission reported in the MEIC inventory for Beijing (227,000 t). Although the total magnitude is consistent, the spatial
346 distribution from top-down estimates differs substantially from bottom-up inventories. Section 3.2.2 further analyzes these

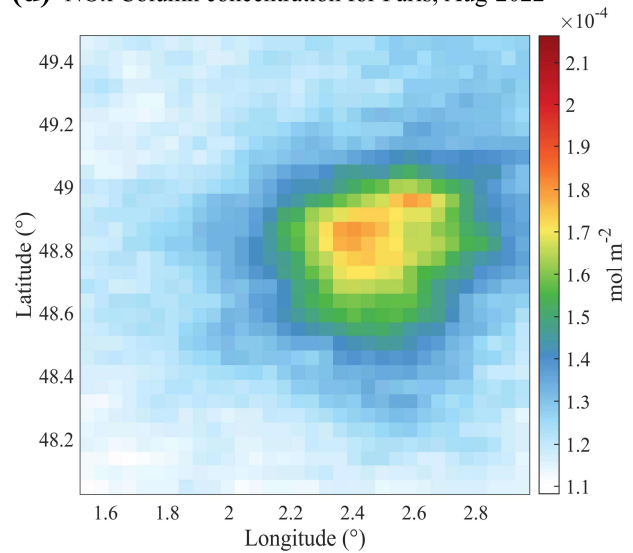
347 differences by simulating urban ffCO₂ plumes using both our ffCO₂ inventory and the ODIAC inventory.

348 By comparison, Paris and Cairo are situated on relatively flat terrain (maximum elevation ~180 m). Terrain-induced wind
349 divergence is negligible relative to total fluxes (wind-terrain and divergence contributions $\sim 10^{-10}$ mol m⁻² s⁻¹), leaving the continuity
350 equation primarily governed by wind-weighted column gradients. Cairo, located upstream of the Nile Delta in a high-albedo desert
351 region, benefits from low uncertainty in satellite-derived NO₂ columns. Under these conditions, the top-down NO_x inventory closely
352 aligns with the bottom-up inventory in terms of spatial distribution. Paris, situated in the Paris Basin along the Seine River,
353 experiences minimal terrain gradients. Although less extreme than Cairo, the slight topographic variation still produces pronounced
354 urban boundary effects in the inversion results.

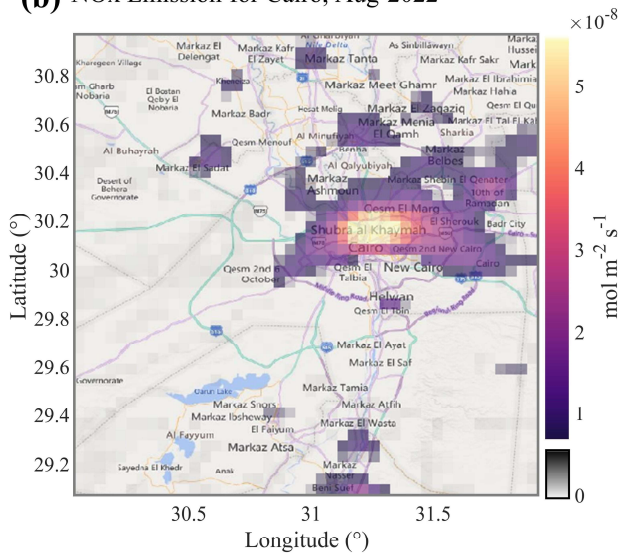
(a) NO_x Emission for Paris, Aug-2022



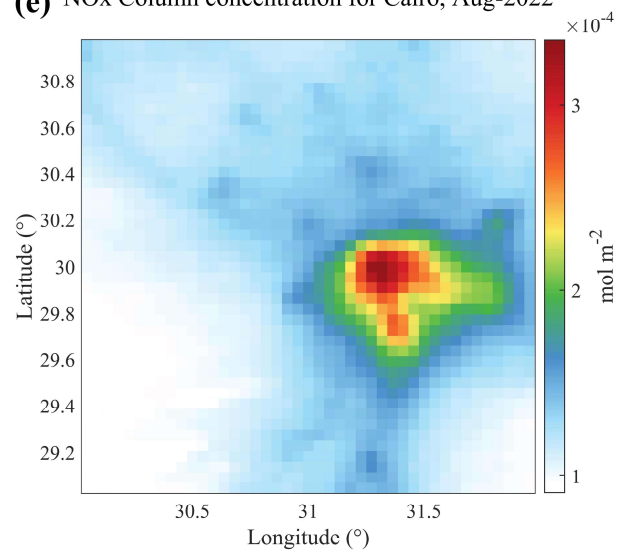
(d) NO_x Column concentration for Paris, Aug-2022



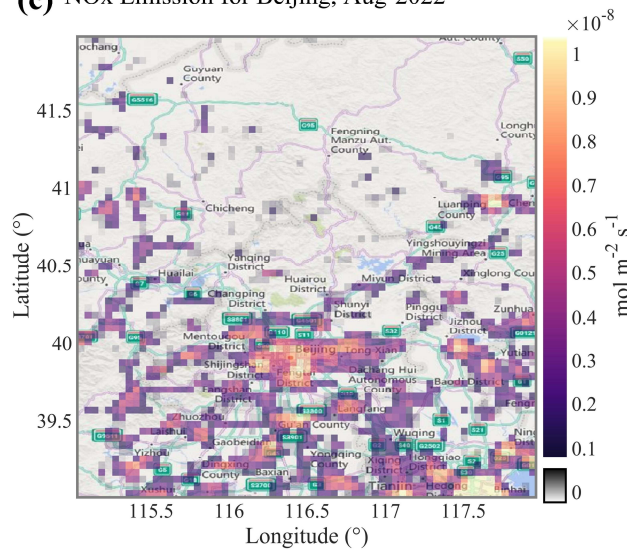
(b) NO_x Emission for Cairo, Aug-2022



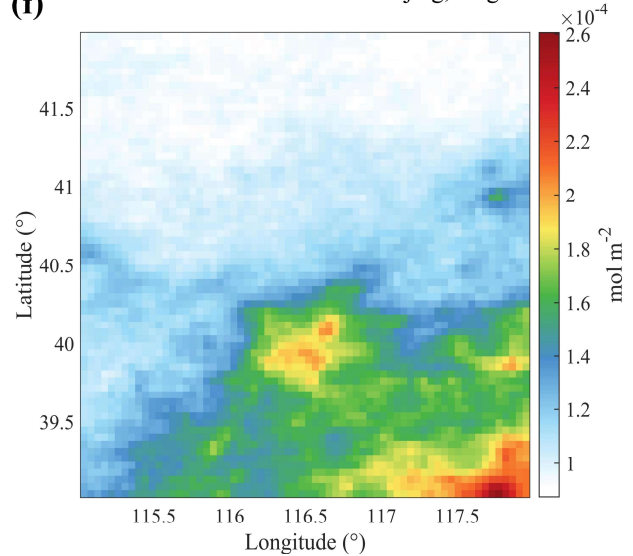
(e) NO_x Column concentration for Cairo, Aug-2022



(c) NO_x Emission for Beijing, Aug-2022



(f) NO_x Column concentration for Beijing, Aug-2022



355
356 **Figure 4** Gridded prior NO_x emission inventories derived from the mass balance method. Panels (a)–(c) show the NO_x flux distributions
357 (unit: mol/m²/s) for Beijing, Paris, and Cairo in August 2022. Panels (d)–(f) present the resampled monthly mean NO₂ column

358 concentration distributions for the three cities. Basemap for panels (a)–(c): Esri World Topographic Map. Sources: Esri, HERE, Garmin,
359 Intermap, INCREMENT P, GEBCO, USGS, FAO, NPS, NRCan, GeoBase, IGN, Kadaster NL, Ordnance Survey, Esri Japan, METI,
360 Mapwithyou, NOSTRA, © OpenStreetMap contributors, and the GIS user community.

361
362 To quantitatively compare the NO_x emission characteristics and atmospheric behavior among Beijing, Paris, and Cairo, derived
363 using the mass balance approach, we analyzed key parameters for August, including mean NO_x fluxes, total emissions, chemical
364 lifetimes, vertical distribution scale heights, and NO_x/NO₂ ratios (Table 1). These NO_x behavior parameters reflect heterogeneous
365 characteristics shaped by the interplay of emission intensity, photochemical conditions, and boundary layer structure.

366 In terms of mean NO_x flux per unit area ($\text{mol m}^{-2} \text{s}^{-1}$), Cairo exhibits the highest value (0.35×10^{-8}), followed by Paris ($0.28 \times$
367 10^{-8}) and Beijing (0.24×10^{-8}), indicating a higher emission of urban emission sources in Cairo—particularly from traffic—resulting
368 in stronger NO_x release per unit surface area. Nevertheless, Beijing’s total NO_x emissions ($182,800 \text{ t yr}^{-1}$) are substantially higher
369 than those of the other two cities, reflecting its larger urban extent and greater overall emission intensity, characteristic of a complex
370 multi-source emission profile.

371 The first-order chemical lifetime of NO_x in the atmosphere indicates its removal rate and is influenced by factors such as OH
372 radical concentration and solar radiation intensity. Paris exhibits the longest NO_x chemical lifetime (6.91 h), followed by Beijing
373 (4.70 h) and Cairo (2.93 h). These differences are closely linked to photochemical activity: strong summer sunlight and high
374 temperatures in Cairo enhance OH-driven removal reactions, whereas the relatively mild mid-latitude climate of Paris, combined
375 with emission control measures, prolongs NO_x lifetime.

376 Regarding vertical distribution, the NO_x scale height also varies across the three cities. Beijing shows the highest scale height
377 (2.08 km), reflecting the combined effects of strong convective transport and multi-source emissions that elevate NO_x into the upper
378 mixing layer. By contrast, Cairo (1.41 km) and Paris (1.21 km) display more typical boundary-layer-constrained distributions,
379 indicating that ground-level emission controls and thermal structure strongly modulate vertical NO_x transport.

380 Finally, the NO_x/NO₂ ratio provides insight into the proportion of NO and its degree of conversion. Beijing exhibits the highest
381 ratio (1.41), followed by Cairo (1.32) and Paris (1.29), suggesting a higher fraction of NO in Beijing, likely associated with dense
382 traffic sources and a larger fraction of primary NO emissions. The relatively lower ratio in Paris reflects a higher NO₂ fraction,
383 consistent with effective emission controls and extensive photochemical conversion.

384
385 **Table 1 Grid-averaged NO_x fluxes, with total urban NO_x emissions as intermediate parameters in the mass balance method.**

City	NO _x average flux mol/(m ² * s)	NO _x total emission kt/month	Chemical lifetime(hour)	Scale height(km)	NO _x /NO ₂
Beijing	0.235×10^{-8}	15.29	4.69	2.07	1.41

Paris	$0.277 \cdot 10^{-8}$	4.45	6.90	1.21	1.29
Cairo	$0.353 \cdot 10^{-8}$	6.78	2.93	1.40	1.32

386 **Details of the uncertainties are provided in the Appendix A5.**

387 **3.2. Urban Fossil Fuel XCO₂ Enhancement (ffXCO₂)**

388 In this section, we summarize the prior ffXCO₂ emissions for each study region. For the selected orbits, the total monthly
389 emissions of Beijing, Paris, and Cairo were approximately 7.47–9.94, 2.91–3.33, and 2.73–3.60 MtC/month, respectively. To
390 constrain emissions, we compared observed and simulated ffXCO₂ enhancements, where ffXCO₂ enhancement is defined as the
391 increase in XCO₂ relative to the background level caused by local fossil fuel emissions. The prior ffXCO₂ enhancements were
392 simulated by taking the inner product of prior NO_x emissions inventories with STILT footprints, while the observed enhancements
393 from DQ-1 were derived by subtracting the background concentration from the measured XCO₂. By comparing prior and observed
394 ffXCO₂ enhancements, we assessed the variability of ffXCO₂ along the orbit and investigated the sources and detectability of the
395 ffXCO₂ signal.

396 **3.2.1. Comparison of Modeled and Observed ffXCO₂**

397 Complex horizontal wind fields can lead to elongated and non-Gaussian plume structures in simulated ffXCO₂ distributions (Ye
398 et al., 2020). This feature is illustrated in Fig. 5c–f. Figures 5a and 5b show the simulated and observed XCO₂ along two overpasses
399 (simulated XCO₂ is obtained by adding the simulated ffXCO₂ to the background derived in Section 2.2.2 (1)). Along these overpasses,
400 ffXCO₂ enhancements exceeding 5 and 10 ppm were observed, with the measured enhancements consistently larger than the
401 simulated values. Although the simulated peak on 7 August is narrower than the observed peak, and the observed peak near 48.4°
402 on 21 August shows a ~0.3° displacement relative to the simulation, the overall magnitude of simulated ffXCO₂ agrees well with
403 observations.

404 To further evaluate the feasibility of constraining fossil fuel CO₂ emissions using the NO_x inventory, we performed a
405 comparative analysis using the ODIAC inventory. We compared simulated ffXCO₂ during the satellite overpasses based on the NO_x
406 and ODIAC inventories (colored shaded areas in the figure), as well as their contributions to the pseudo-observed XCO₂ at the
407 satellite locations (colored dots), where the red line represents enhancements derived from the NO_x inventory and the green line
408 represents those from ODIAC. Over Paris, the NO_x-based simulation yields higher ffXCO₂ enhancements than ODIAC, likely due
409 to uncertainty in the prior CO₂-to-NO_x ratio. Nonetheless, both inventories capture enhancements exceeding 4 ppm. Moreover, the
410 line plots indicate that the temporal variation and magnitude of the simulated concentration contributions (red and green lines) are
411 nearly identical.

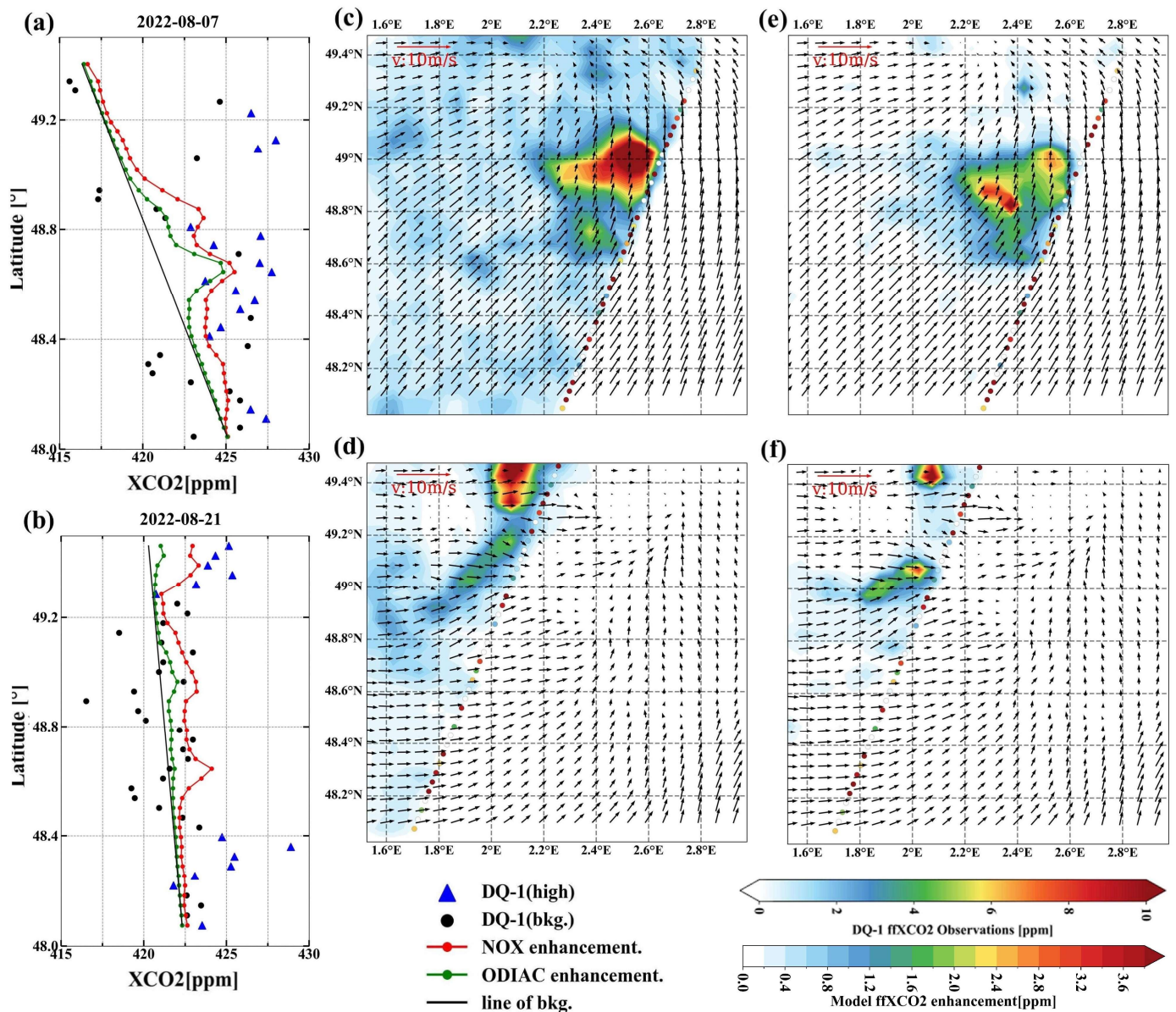
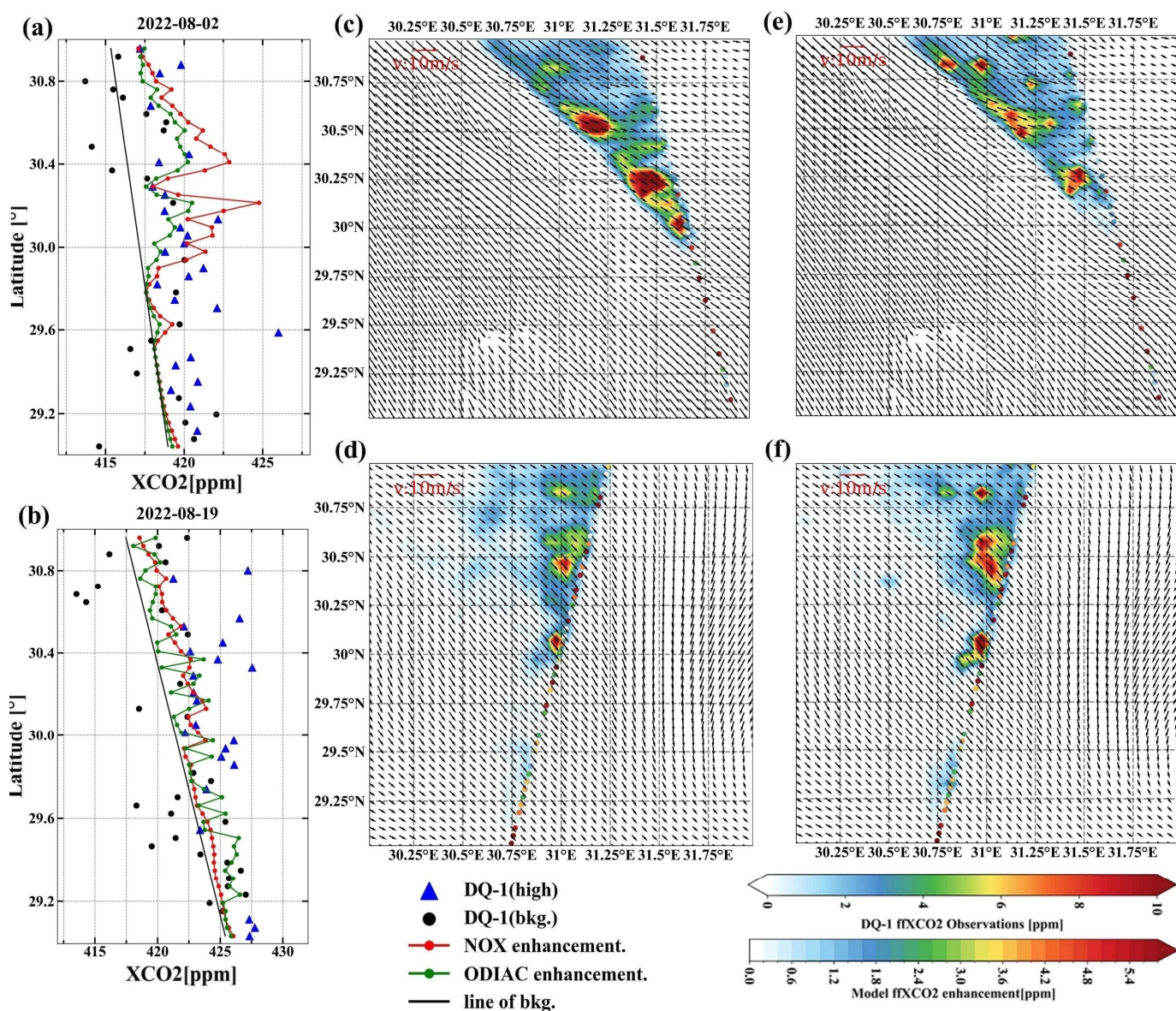


Figure 5 Comparison between simulated and observed fXCO₂ enhancements using DQ-1 overpasses above Paris on 7 August 2022 and 21 August 2022 at 01:00 UTC. Panels (a) and (b) show DQ-1 XCO₂ along the two tracks (black dots and blue triangles) and simulated XCO₂ (red solid line: sum of background concentration and fXCO₂ simulated using the NO_x emissions; green solid line: sum of background concentration and fXCO₂ simulated using the ODIAC inventory), averaged over 0.5 s. Black circles denote the data used to derive the background concentration (black solid line). Panels (c)–(f) show simulated fXCO₂ and observed fXCO₂ retrieved from DQ-1 data ((c), (d): based on the NO_x inventory; (e), (f): based on the ODIAC inventory). Background XCO₂ concentrations have been subtracted. The reference vector indicates a wind speed of 10 m/s.

We examined local fXCO₂ enhancements during two overpasses of Cairo on 2 August 2022 at 11:00 and 19 August 2022 at 23:00. As shown in Fig. 6, the simulated fXCO₂ peaks exceed 6 ppm. In contrast to Paris, where enhancements are widespread, diffuse, and lack clear structure, and Beijing, where plumes exhibit complex patterns, the simulated fXCO₂ over Cairo is strongly influenced by northwesterly winds, resulting in well-defined plumes. Figure 5a illustrates that the simulations based on both inventories on 2 August produce similar magnitudes and trends, consistent with the Paris results, where the NO_x-based simulation

426 exceeds that from ODIAC. Notably, the simulated peaks on 2 August also show a spatial offset relative to the observations.
 427 Following Ye et al. 2020, such offsets are attributed to the satellite trajectory crossing the plume edges nearly parallel to the plume
 428 axis, making the simulated ffXCO₂ highly sensitive to errors in the horizontal wind field.

429 Notably, the overpasses above Paris and Cairo (Figs. 5a and 6b) exhibit higher latitudinal gradients in the background XCO₂,
 430 as indicated by the background lines. The approach used to derive these background lines provides a reliable estimate of background
 431 XCO₂ because, within the relevant regions, the observed and modeled cumulative ffXCO₂ enhancements along the satellite track
 432 are largely consistent. Consequently, these findings highlight the effectiveness of the background line method for inferring satellite-
 433 observed background XCO₂. They also emphasize that the spatial scale of satellite data analysis is closely linked to the constraints
 434 imposed by local emission sources. Neglecting the latitudinal gradient of background XCO₂ may introduce biases in the estimation
 435 of ffXCO₂ and, consequently, in derived emission fluxes(Ye et al., 2020).

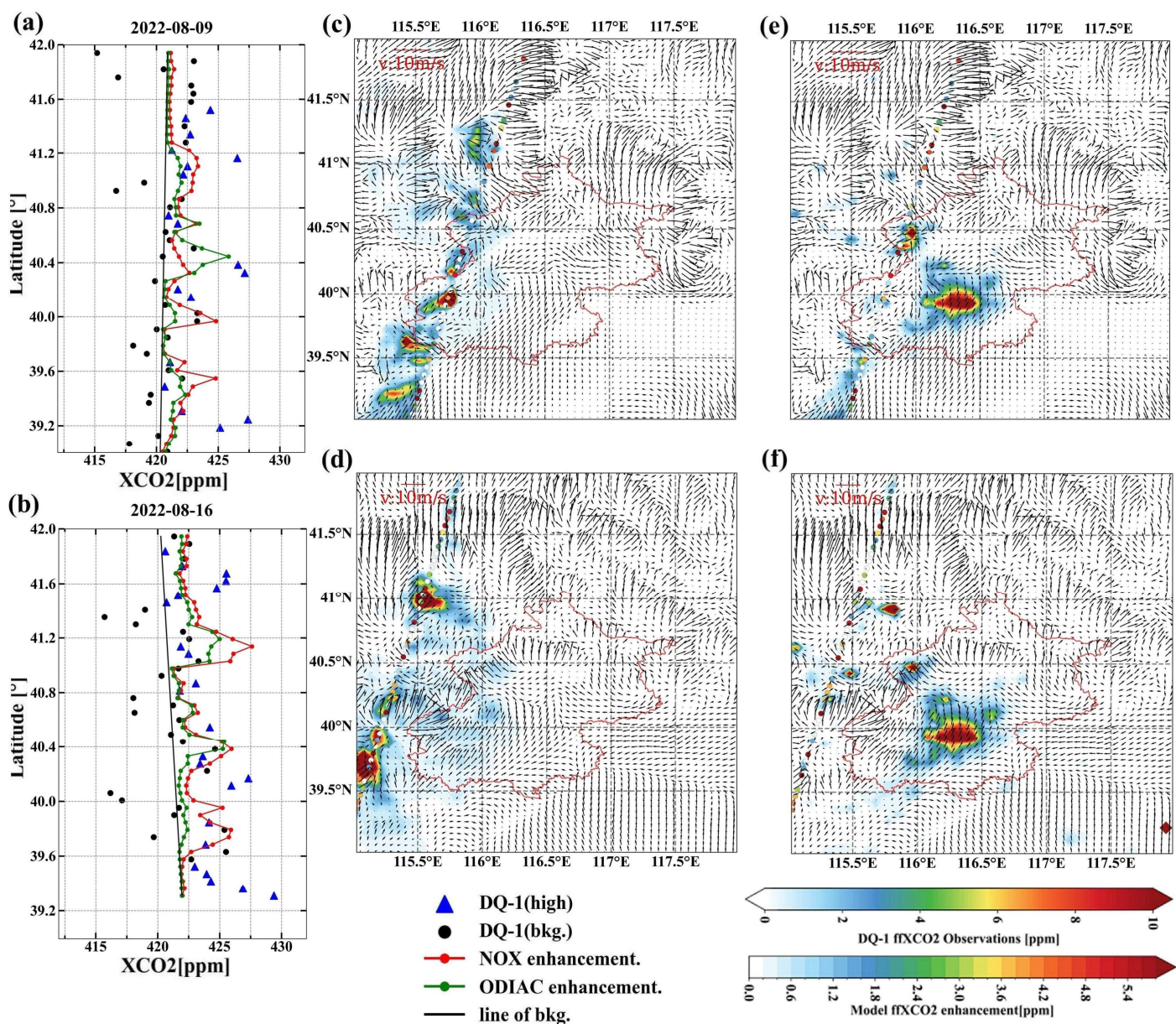


436
 437 **Figure 6** Similar to Fig. 5, comparison between simulated and observed ffXCO₂ enhancements using DQ-1 overpasses above Cairo on 2
 438 August 2022 at 11:00 UTC (panels a, c, e) and 19 August 2022 at 23:00 UTC (panels b, d, f). Panels (c) and (d) show the simulated ffXCO₂

439 enhancements based on the NO_x emissions, while panels (e) and (f) show those based on the ODIAC inventory.

440

441 3.2.2. Comparison of NO_x and ODIAC Modeled ffXCO_2 in Beijing



442

443 Figure 7 Similar to Fig. 5, comparison between simulated and observed ffXCO_2 enhancements using DQ-1 overpasses above Beijing on 9
444 August 2022 at 18:00 UTC (panels a, c, e) and 16 August 2022 at 18:00 UTC (panels b, d, f). Panels (c) and (d) show the simulated ffXCO_2
445 enhancements based on the NO_x emissions, while panels (e) and (f) show those based on the ODIAC inventory.

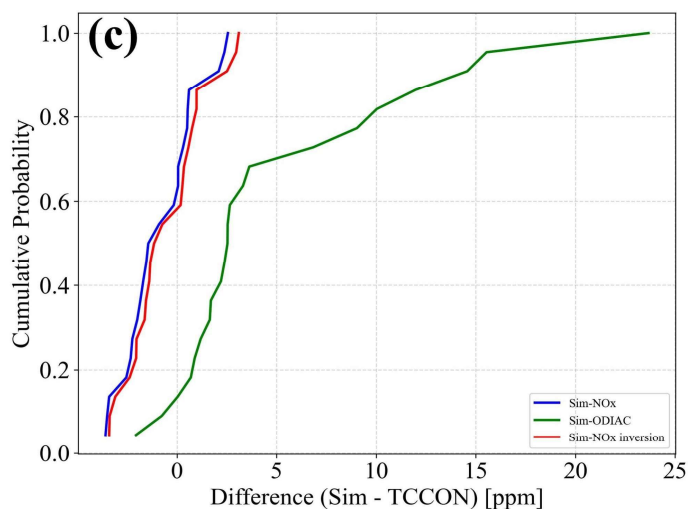
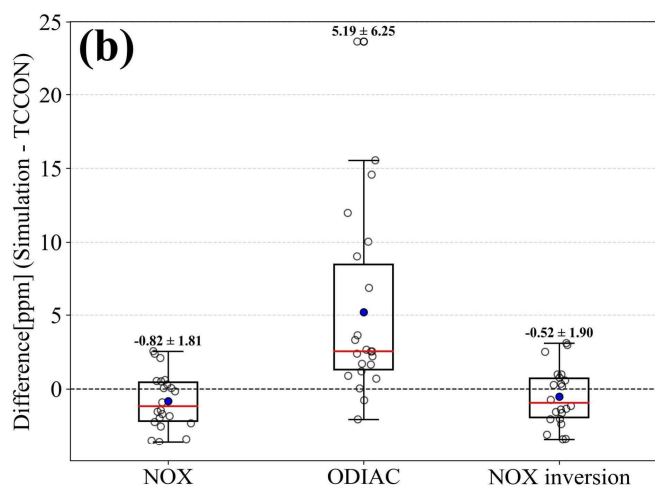
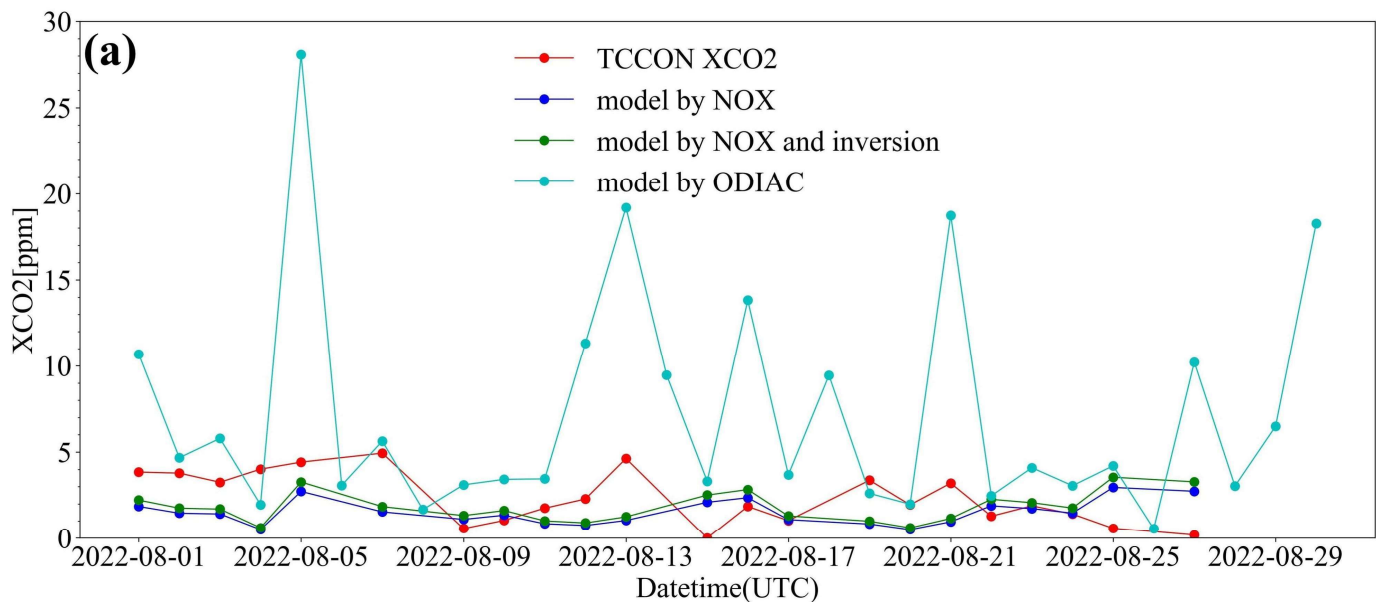
446

447 Figure 7 illustrates the investigation of local ffXCO_2 enhancements over Beijing using two DQ-1 overpasses and corresponding
448 simulated ffXCO_2 . In the figure, the colored shading represents XCO_2 concentrations accumulated over the previous 24 hours
449 simulated by STILT, while the colored dots indicate satellite-observed XCO_2 enhancements, calculated by subtracting the

450 background values (see Section 2.2.2). The red contours outline the urban area of Beijing. As shown, ffXCO₂ over this region can
451 reach approximately 6.0 ppm.

452 Notably, simulations based on the NO_x inventory (Figs. 7c, d) show that the spatial distribution of ffXCO₂ enhancements varies
453 significantly with meteorological conditions and emission patterns. In contrast, for Paris and Cairo, the simulated ffXCO₂ is more
454 concentrated. Over Beijing, however, the ffXCO₂ distribution is more dispersed and comprises multiple plumes. When comparing
455 simulations using NO_x and ODIAC inventories for Paris and Cairo, the overall plume structures remain largely unaffected. Over
456 Beijing, the simulations using the ODIAC inventory (Figs. 7e, f) display an almost identical ffXCO₂ enhancement distribution across
457 different wind conditions, showing pronounced anomalies in the urban area. Such similarity is unrealistic.

458 We attribute this behavior to the ODIAC inventory allocating disproportionately high fossil fuel emissions to central Beijing.
459 When STILT footprints intersect the urban area, the high emission gradients in ODIAC (central urban emissions far exceeding
460 suburban values) amplify ffXCO₂ enhancements in the inner city. ODIAC's low-emission thresholds are influenced by nighttime
461 light saturation, with median differences ranging from 47% to 84%. Consequently, ODIAC artificially concentrates emissions in the
462 city center while underrepresenting surrounding suburban areas. This makes it challenging to accurately constrain CO₂ fluxes in the
463 peripheral regions using ODIAC. Observations from the TCCON Xianghe site further highlight the limitations of ODIAC's emission
464 allocation in the Beijing area.



465
 466 **Figure 8 Comparison of ffXCO₂ observed at the TCCON Xianghe site in Beijing during August with ffXCO₂ simulated using the NO_x**
 467 **inventory and the ODIAC inventory. Panel (a) shows the ffXCO₂ observed by TCCON (red line), simulated ffXCO₂ using the NO_x**
 468 **emissions (dark blue line), simulated ffXCO₂ using the ODIAC inventory (light blue line), and simulated ffXCO₂ using the posterior NO_x**
 469 **emissions (green line). Panel (b) presents the distribution of differences between simulated ffXCO₂ (from the NO_x and ODIAC inventories)**
 470 **and TCCON observations throughout August, with bold numbers indicating the mean and standard deviation. Panel (c) shows the**
 471 **cumulative probability distributions of the differences between simulated ffXCO₂ (NO_x emissions and ODIAC inventory) and TCCON**
 472 **observations.**

473
 474 Figure 8 presents the comparison of August ffXCO₂ at the TCCON site with simulations using the ODIAC and NO_x inventories.
 475 Unlike the ffXCO₂ calculation described in Section 2.2.2, the TCCON observations provide daily-averaged fossil fuel CO₂
 476 enhancements, where TCCON ffXCO₂ is calculated as TCCON XCO₂ minus background XCO₂ and NEE contributions (details in
 477 the Appendix A3). In Figure 8a, the dark blue line represents ffXCO₂ simulated at the TCCON site using the NO_x inventory, the
 478 green line shows the ffXCO₂ simulated after optimization with the inversion using DQ-1 observations, the light blue line corresponds
 479 to ODIAC-based simulations, and the red line depicts TCCON-observed ffXCO₂.

480 Figure 8b quantifies the accuracy of the simulations by plotting the difference between the simulated ffXCO₂ and TCCON
 481 observations on the same day and summarizing the monthly mean and standard deviation. The monthly mean absolute difference
 482 for the NO_x inventory is 0.82 ppm, while ODIAC exhibits a much larger discrepancy of 5.19 ppm. The inversion-constrained NO_x
 483 inventory reduces the mean absolute difference to 0.52 ppm, closely matching TCCON observations. Figure 8c shows the
 484 cumulative probability distribution of the differences between simulated and observed ffXCO₂. The differences for the NO_x and
 485 inversion-constrained NO_x simulations are largely centered around zero (blue and red lines), whereas for ODIAC, approximately
 486 30% of differences exceed 5 ppm.

487 These results indicate that for Beijing in August, simulations based on the NO_x inventory outperform those using ODIAC.
 488 Given that the prior ffCO₂ emissions in both inventories are of similar magnitude, the observed discrepancies are primarily
 489 attributable to the spatial allocation of emissions in ODIAC. The combined inversion using TROPOMI and ACDL data provides a
 490 more accurate reconstruction of urban ffXCO₂ plume structures.

491 3.2.3. ffCO₂ Inversion Results

492 **Table 2 Results of inversion of for CO₂-to-NO_x ratio selected cities using DQ-1 XCO₂ data**

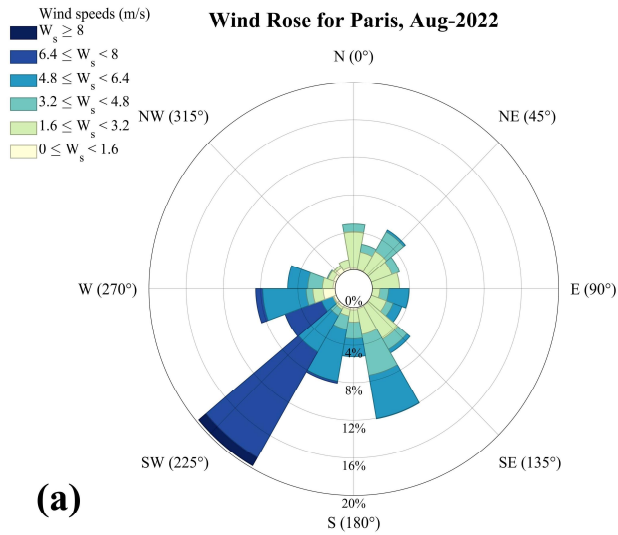
City	Overpass	Prior CO ₂ -to- NO _x ratio (λ)	Prior uncertainty (%)	Observation uncertainty (ppm)	Model transport uncertainty (ppm)	Posterior CO ₂ -to-NO _x ratio (λ) and uncertainty
Cairo	2022/08/02	470	40.59%	1.23	1.75	428±64.58
	2022/08/19			1.06	2.10	512±96.56
Paris	2022/08/07	601	30.12%	2.45	0.36	731±107.60
	2022/08/21			1.68	0.76	742±138.53
Beijing	2022/08/09	694	28.12%	2.31	1.28	640±90.11
	2022/08/16			1.79	3.25	553±89.80

493 This section presents the inversion results of urban carbon emissions for Cairo, Paris, and Beijing, based on TROPOMI and
 494 DQ-1 satellite overpass observations (see Table 2). In the inversion, we systematically accounted for observational errors and
 495 uncertainties in atmospheric transport to improve the reliability of the emission estimates. From the posterior results, we derived
 496 city-specific CO₂-to-NO_x ratios and, by combining them with TROPOMI-derived NO_x emissions, further quantified fossil fuel CO₂
 497 (ffCO₂) emissions. This approach not only enables quantitative assessment of emissions but also provides a scientific basis for cross-
 498 city comparisons of emission characteristics, while demonstrating the potential of multi-satellite data for urban emission monitoring.

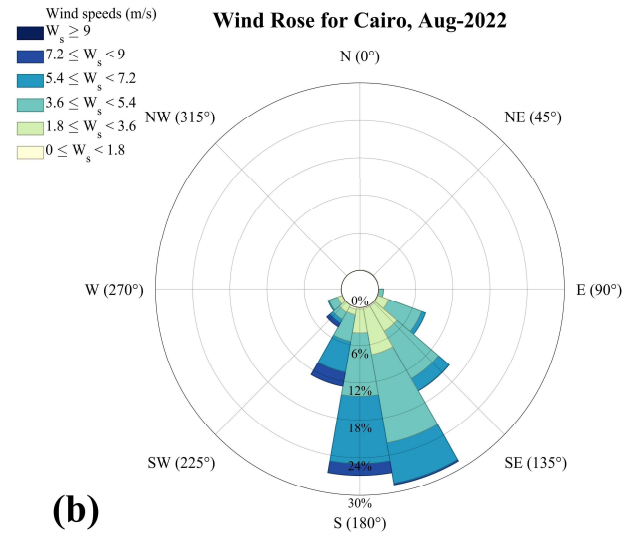
499 For the selected orbits, the posterior CO₂-to-NO_x ratios were 428–512 for Cairo, 731–742 for Paris, and 553–640 for Beijing

(Table 2). These ratios exhibited clear temporal variability under different background conditions. The magnitude of emissions captured by each orbit depended strongly on its distance from major emission regions and the contemporaneous domain-averaged wind conditions (Che et al., 2022). The domain-averaged wind speeds for the study month (Fig. 9), as well as the high-resolution wind fields at overpass time (black arrows in Figs. 5–7), were consistently greater than 3 m s^{-1} . Under such meteorological conditions, the posterior estimates represent emissions from several hours prior to satellite overpass. The posterior uncertainties of the CO_2 -to- NO_x ratio were 15.09%–18.86% for Cairo, 14.72%–18.67% for Paris, and 14.08%–16.24% for Beijing. Overall, uncertainties were larger for Cairo and Paris compared with Beijing.

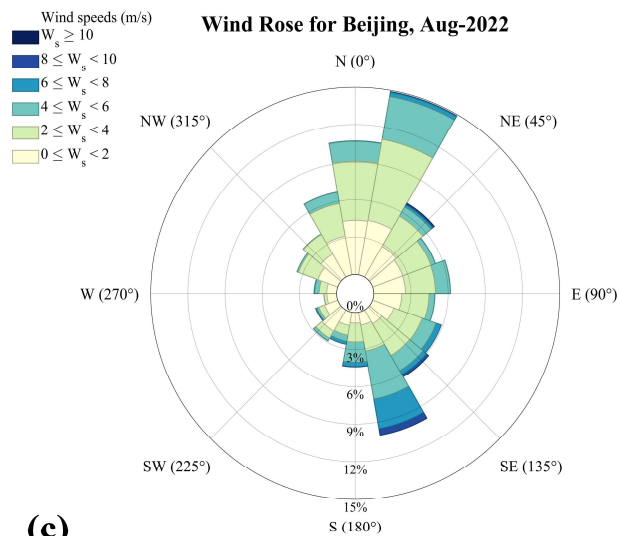
As described in section 4.1, the prior uncertainty of the CO_2 -to- NO_x ratio was prescribed based on available statistics and emission characteristics. Owing to more comprehensive statistics and advanced manufacturing processes, large metropolitan areas typically exhibit better-characterized emission features. Accordingly, the prior uncertainties for Beijing and Paris were smaller than those for Cairo. Table 2 further shows that the relative contributions of observational and transport errors differed across cities. In Cairo, transport errors dominated over observational errors, whereas in Paris the opposite held true. For Beijing, the relative magnitudes of transport and observational errors varied across orbits. The overall smaller posterior uncertainty for Beijing compared to Cairo and Paris reflects its more stable prior emission characteristics.



(a)



(b)



(c)

Figure 9 Monthly mean wind rose plots for Cairo, Paris, and Beijing in August.

3.3. The Uncertainty of Transport Model

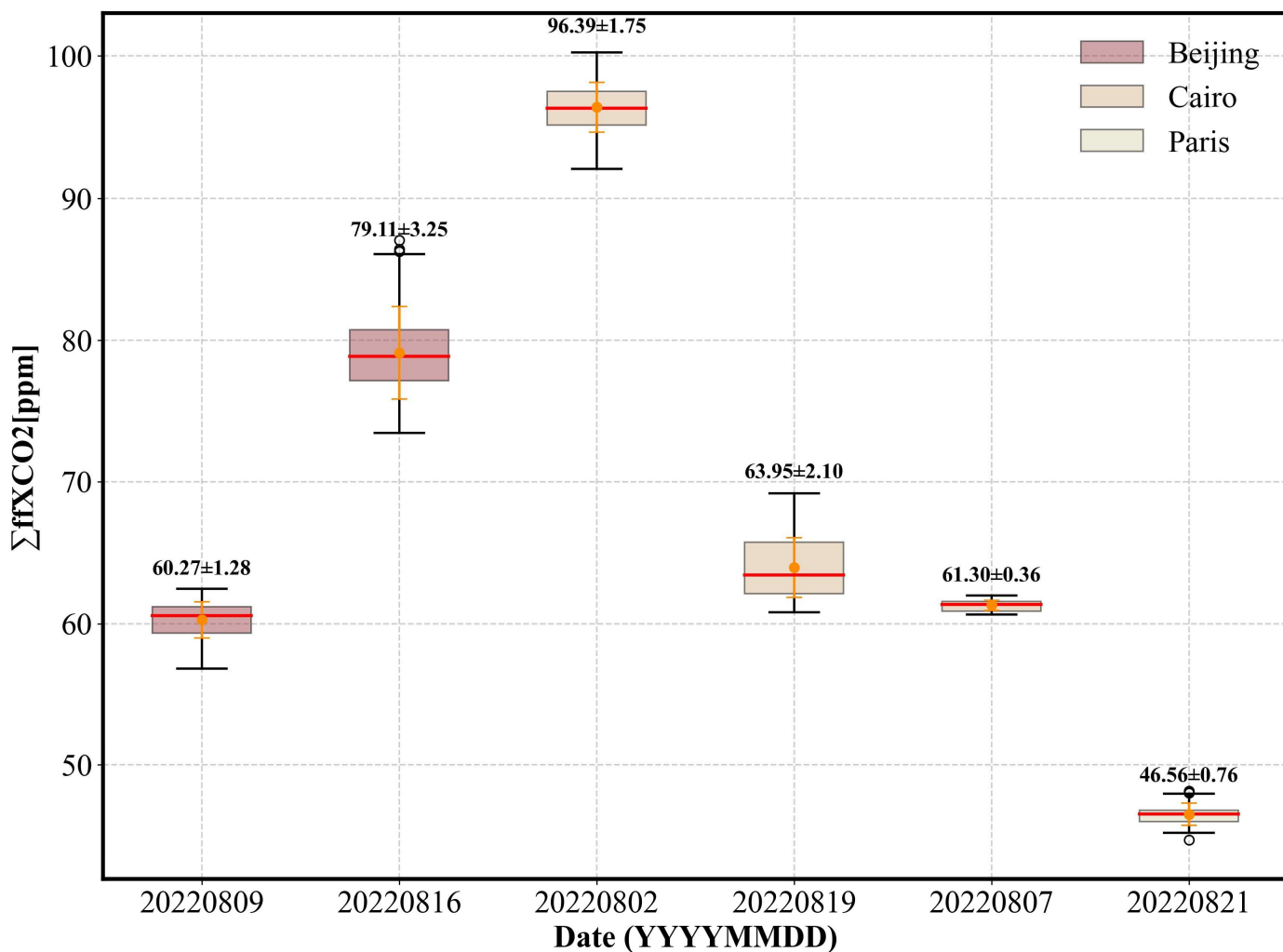
Atmospheric transport modeling uncertainty has been recognized as a major factor affecting emission constraints (Wu et al., 2018). Systematic errors arising from a combination of transport model biases and misrepresented statistical inputs can reduce the magnitude and spatial coverage of terrestrial uncertainty reductions by roughly a factor of two (Wang et al., 2014). Notably, transport-related uncertainties in ffXCO₂ represent a key source of error in inverse emission estimates (Ye et al., 2020). In this section, we quantify the impact of transport errors on simulated XCO₂ arising from uncertainties in horizontal wind fields and vertical mixing, with a focus on their influence on the inversion of ffXCO₂ fluxes.

Errors induced by wind field uncertainties propagate through the model and affect the accuracy of CO₂ emission estimates (Sheng et al., 2025). Previous studies have accounted for column transport errors by weighting variance relative to pressure and treating each model level independently (Lin and Gerbig, 2005; Wu et al., 2018). Ye et al. 2020 further quantified ffXCO₂

526 simulation uncertainty by introducing random perturbations in wind speed and direction. Building on these approaches, we
 527 investigate how horizontal wind speed and wind direction errors influence inversion performance.

528 Here, horizontal transport error is propagated through the model via its effect on ffXCO₂ plume dispersion. For the selected
 529 cities, errors are assumed to be unbiased. Wind direction uncertainty is represented by rotating the plume around the emission center,
 530 followed by the addition of random wind speed perturbations to the rotated plume. Using DQ-1 wind field data, random errors were
 531 added at each model level (wind direction perturbation between -10° and 10°, wind speed perturbation between -1 m/s and 1 m/s),
 532 and the STILT footprints were recomputed to obtain plume-averaged footprints with random errors included(Yi et al., 2024).

533 In total, 10⁴ simulations were conducted, with the ffXCO₂ integrated along each satellite track. The standard deviation (1σ) of
 534 these simulations is used to represent the uncertainty in simulated ffXCO₂ resulting from horizontal transport errors (Figure 10).



535
 536 **Figure 10** Boxplots of modeled integrated ffXCO₂ enhancements ffXCO₂ along selected DQ-1 overpasses for the three cities (distinguished
 537 by box color) with dates labeled on the x-axis. For each box, the central line represents the median (q2), and the bottom and top edges
 538 represent the 25th and 75th percentiles (q1 and q3), respectively. Whiskers extend to the minimum and maximum values. Numbers
 539 indicate the mean ± standard deviation.

540
 541 Figure 10 presents the total simulated ffXCO₂ along DQ-1 overpasses for the different study regions. Overall, the simulated

ffXCO₂ totals for the three cities are of comparable magnitude. Notably, compared with Beijing and Cairo, the horizontal transport uncertainty along the two Parisian tracks is the lowest, at 0.36 ppm and 0.76 ppm, respectively. In Cairo, the satellite tracks traverse the edges of emission plumes, making the simulations highly sensitive to wind speed and direction, which results in larger transport model errors. Beijing, with its complex terrain and variable wind fields, exhibits more intricate transport uncertainties relative to the other two cities. These observations indicate that transport model uncertainty is closely related to city-scale emissions, the relative alignment of plumes and satellite tracks, model performance, and local topography. Variations in these factors contribute to temporal changes in posterior emission uncertainties along different tracks.

Vertical turbulent mixing governs the vertical transport of air parcels and controls the dilution of surface emissions within the boundary layer (Vertical mixing in atmospheric tracer transport models: error characterization and propagation). Although column-integrated measurements may be less sensitive to the vertical distribution of tracers than in situ observations, errors in planetary boundary layer (PBL) height can still affect column simulations due to wind shear and its interaction with vertical redistribution of tracers (Planetary boundary layer errors in mesoscale inversions of column-integrated CO₂ measurements). It is worth noting that the ACDL instrument includes an aerosol channel capable of providing extinction coefficient profiles and planetary boundary layer height (PBLH) products (Dai et al., 2024). In this study, PBLH data derived from ACDL retrievals are used in the simulations, helping to mitigate errors arising from inaccurate boundary layer height assumptions. Therefore, boundary layer height errors are not considered in the estimation of ffXCO₂.

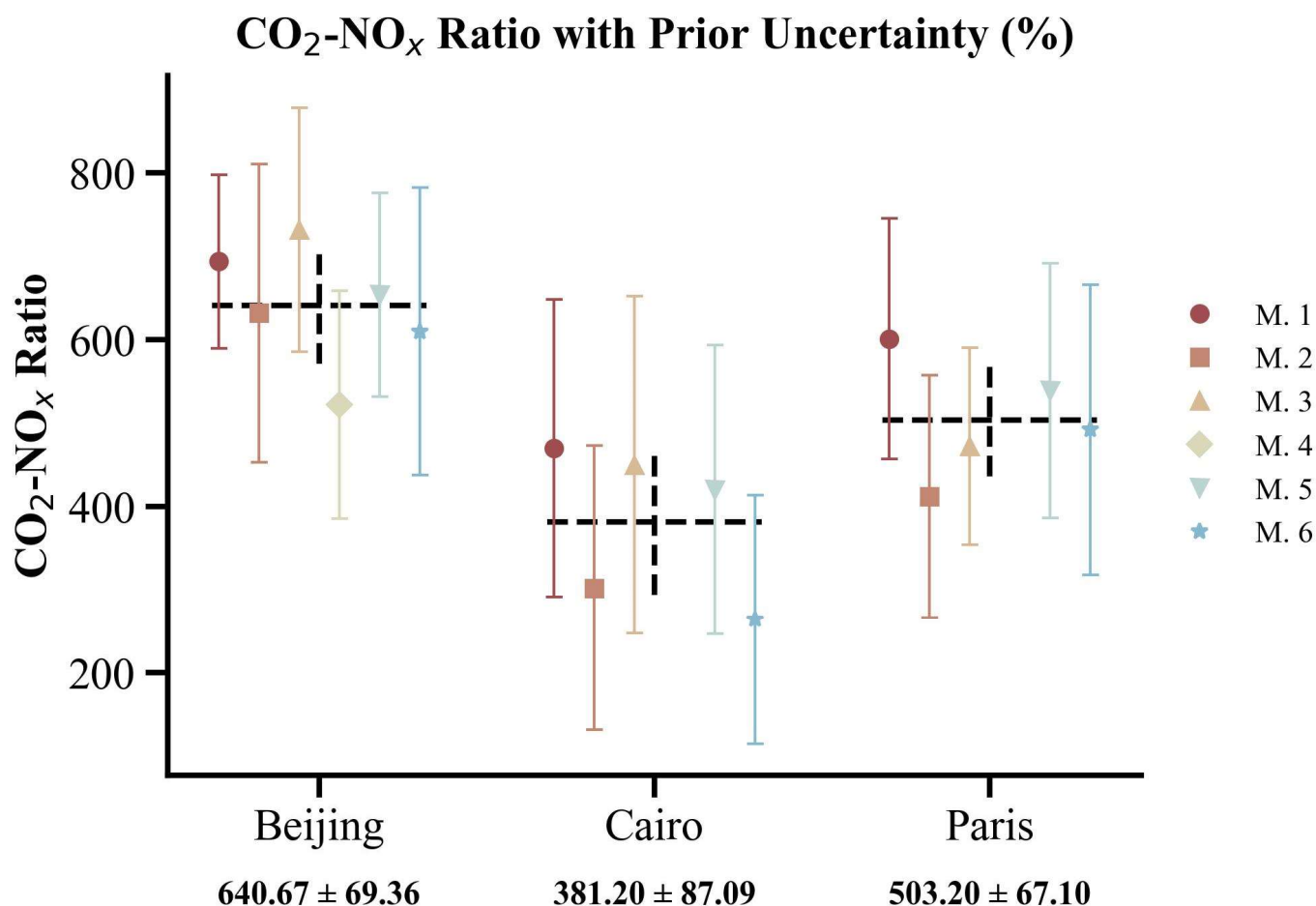
4. Importance of Satellite Observations for Optimizing the CO₂-to-NO_x Ratio

4.1. Variations in CO₂-to-NO_x ratio calculation methods

We systematically accounted for the uncertainties associated with the prior CO₂-to-NO_x ratios for each method (see Section 2.2.1 (4) M1-M6). The uncertainty of the CO₂-to-NO_x ratio arises from the uncertainties of the underlying emissions. For Method 1, a Monte Carlo simulation was performed: CO₂ and NO_x inventory uncertainties (Wang et al., 2013; Huang et al., 2017) were used to generate random perturbations at each grid, and the CO₂-to-NO_x ratio was recalculated 10,000 times to obtain the distribution characteristics. The prior CO₂-to-NO_x ratio uncertainty was expressed as R90/M, where R90 is the range between the 95th and 5th percentiles and M is the median value from 10,000 Monte Carlo simulations. For Method 2, the uncertainty was represented as:

$$\sigma_{C/N} = \sqrt{\sigma_{NO_x}^2 + \sigma_{FFCO_2}^2} \quad (14)$$

where σ_{NO_x} and σ_{FFCO_2} denote the uncertainties of the NO_x and ffCO₂ emission factors, respectively. Notably, for each method, the use of different inventories requires adjustment of the assigned uncertainties (see Appendix A6). In Method 3, the prior CO₂-to-NO_x ratio uncertainty was derived from the quadratic sum of observational uncertainties in NO₂ and CO₂ concentrations and



571

572 **Figure 11 Results of CO₂-to-NO_x ratios obtained using different calculation methods for Beijing, Cairo, and Paris. Different CO₂-to-NO_x**
 573 **ratios within the same city are distinguished by color. Additionally, the mean and standard deviation of the different ratios for each city**
 574 **are also shown.**

575

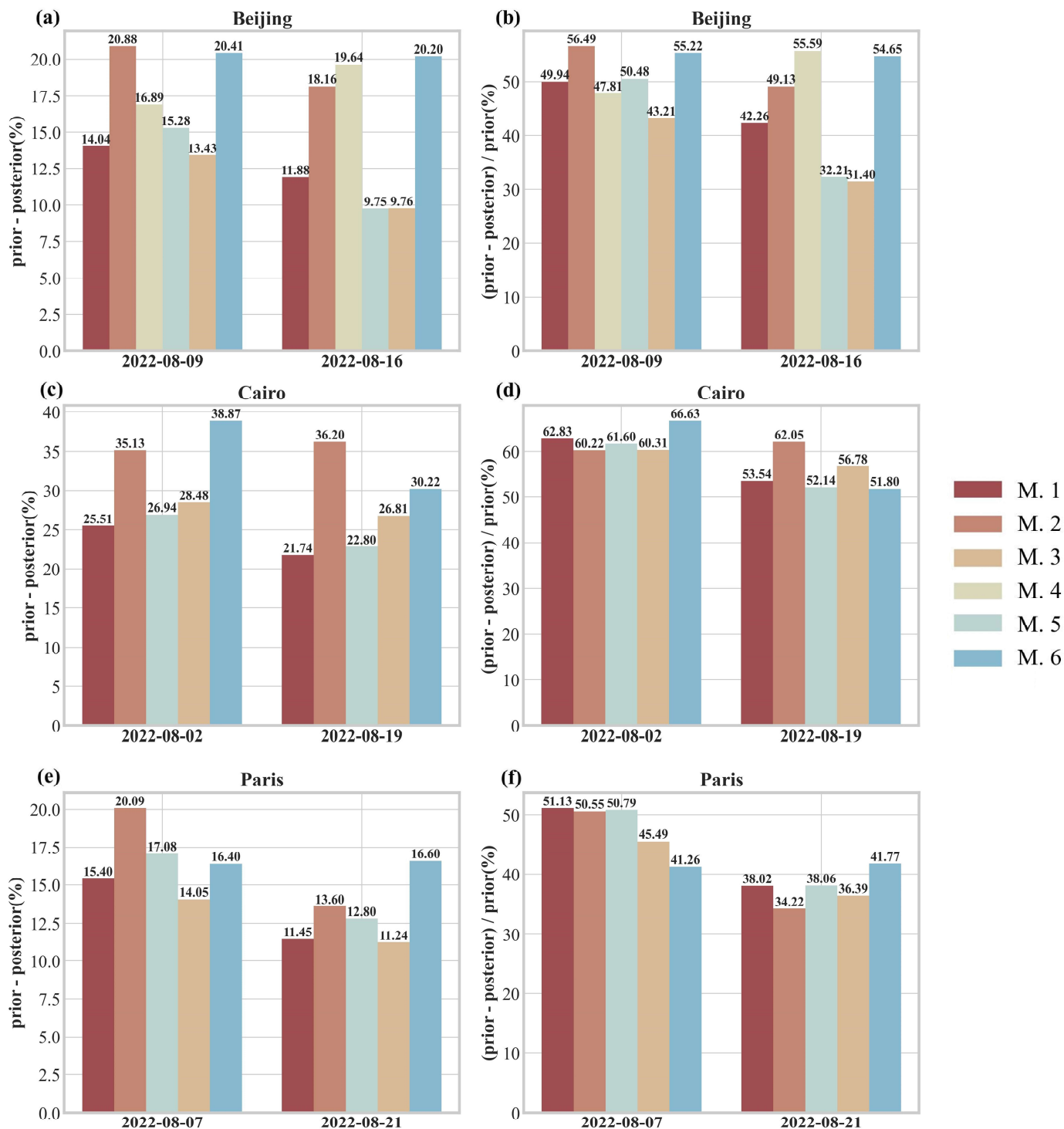
576 In this section, we used six different CO₂-to-NO_x ratio calculation methods to estimate the city-scale ratios for Beijing, Cairo,
 577 and Paris in August. Since the MEIC inventory is only available for Beijing, six prior CO₂-to-NO_x ratios were obtained for Beijing,
 578 while five ratios were derived for Paris and Cairo. Figure 11 presents the CO₂-to-NO_x ratios and their associated uncertainties for
 579 each city using the different methods. We also calculated the mean and standard deviation of the ratios across methods for each city,
 580 reflecting both the overall understanding of the city-scale prior CO₂-to-NO_x ratio and the variability arising from methodological
 581 differences.

582 The results consistently show the ordering Beijing > Paris > Cairo. Moreover, more developed cities typically have better
 583 production technologies and more detailed emission statistics(Oda et al., 2019; Ye et al., 2020). Consequently, the prior uncertainties
 584 for Beijing and Paris are notably smaller than those for Cairo, and the variability of CO₂-to-NO_x ratios across methods is also reduced
 585 for these cities.

4.2. Bayesian Inversion for Reducing CO₂-to-NO_x Ratio Uncertainty

Using different prior CO₂-to-NO_x ratios, we conducted the Bayesian inversion described in Section 2.2.2 to optimize the August CO₂-to-NO_x ratios for Beijing, Cairo, and Paris along the respective DQ-1 satellite overpasses. Figure 12 shows the absolute reduction in posterior uncertainty (posterior minus prior) and the relative reduction (prior minus posterior, divided by prior) for each city across different orbits. For Beijing, the posterior uncertainty decreased by 9.75%–20.88%, corresponding to a 31.4%–56.49% reduction relative to the prior. In Cairo, the posterior uncertainty decreased by 21.74%–38.87%, equivalent to a 51.8%–66.63% reduction, while in Paris the reduction ranged from 11.24% to 20.09%, corresponding to a 34.22%–51.13% decrease relative to the prior.

These results indicate that, for all cities, the posterior uncertainties were significantly reduced regardless of the method used to calculate the prior ratio. This demonstrates that constraining the inversion with DQ-1 ACDL observations substantially improves the accuracy of ffCO₂ estimates derived from NO_x emissions. Notably, in Cairo—the city with the largest prior uncertainty—the reduction in uncertainty after constraining with both active and passive satellite observations was the greatest, highlighting the effectiveness of satellite data in mitigating emission uncertainties in cities with incomplete statistical information. These findings underscore the potential of satellite remote sensing to supplement emission inventories and enhance the reliability of urban emission estimates.

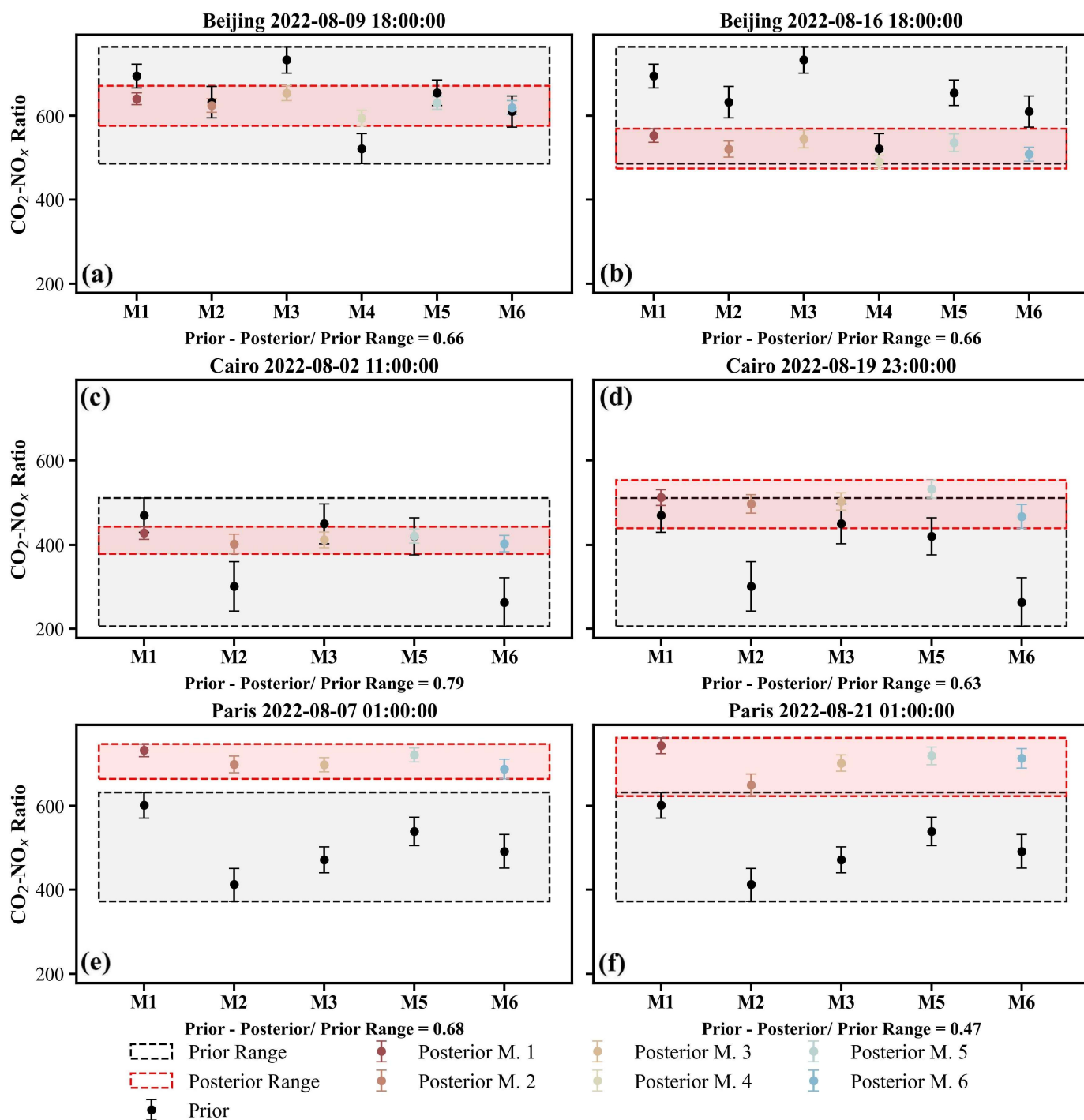


601
602 **Figure 12 Comparison of Bayesian inversion prior and posterior uncertainties for each orbit over different cities. Panels (a), (c), and (e)**
603 **show the absolute reduction in uncertainty (prior uncertainty minus posterior uncertainty), while panels (b), (d), and (f) show the relative**
604 **reduction in uncertainty (prior minus posterior uncertainty divided by prior uncertainty). Results from different prior CO₂-to-NO_x ratios**
605 **are represented by bars in different colors, with the values displayed at the top of each bar.**

606
607 Furthermore, we examined the range of CO₂-to-NO_x ratios calculated for each city using different methods (Fig. 13). In the
608 figure, the black boxes represent the prior distribution ranges, while the red boxes indicate the posterior distribution ranges. The
609 distribution ranges illustrate the variability among CO₂-to-NO_x ratios obtained from different methods, and we also quantified the

610 reduction of the posterior range relative to the prior. Except for the orbit over Paris on 21 August, all other results show that the
 611 posterior ranges were reduced by more than 60% compared to the priors.

612 These results demonstrate that our approach effectively reduces the discrepancies arising from different CO₂-to-NO_x ratio
 613 calculation methods. That is, prior ratios derived from various methods are constrained to approximately the same range after
 614 inversion. This finding underscores the importance of using observational constraints to obtain more accurate CO₂-to-NO_x ratios in
 615 future ffCO₂ emission estimations.



616
 617 **Figure 13** Distribution ranges of prior and posterior CO₂-to-NO_x ratios calculated using different methods. Black boxes represent the
 618 range of prior CO₂-to-NO_x ratios, with posterior ratios indicated by black circles. Red boxes represent the range of posterior CO₂-to-NO_x

619 ratios, with posterior uncertainties from different methods shown using different colors and symbols.

620 5. Summary

621 Accurate identification and quantification of anthropogenic CO₂ emissions form a critical scientific basis for national emission
622 reduction policies and carbon sink strategies. However, bottom-up inventory approaches typically operate on long compilation
623 cycles (e.g., annual), making it difficult to capture short-term or near-real-time emission dynamics. Most inventories provide only
624 annual totals and lack the temporal resolution needed to characterize daily, hourly, or event-driven emissions.

625 In this study, we developed a city-scale ffCO₂ inversion framework that integrates both active and passive satellite observations
626 of greenhouse gases. This framework enables high-resolution estimation of fossil fuel emissions at satellite overpass times and over
627 preceding hours, while simultaneously constraining the city-scale CO₂-to-NO_x ratio. A key feature of the approach is its reduced
628 reliance on prior emission inventories, allowing rapid and objective identification and quantification of anthropogenic emission
629 signals at regional scales, thereby enhancing the monitoring and verification of urban emission dynamics. In this framework,
630 satellite-observed XCO₂ enhancements attributed to urban emissions are used to constrain WRF-STILT atmospheric transport
631 simulations of anthropogenic CO₂. This process not only enables quantitative assessment of urban fossil fuel emissions but also
632 provides independent evidence for improving emission inventories and refining urban carbon accounting systems. The study
633 highlights the potential of combining multi-source satellite observations with transport models and lays a foundation for future city-
634 scale ffCO₂ inversions based on the CO₂-to-NO_x ratio. Furthermore, we discuss the impact of the lack of standardized CO₂-to-NO_x
635 ratio calculation methods on urban emission estimates and demonstrate that observational constraints on city-scale ratios can
636 substantially improve ffCO₂ estimation from a carbon-nitrogen co-optimization perspective. Using a Bayesian inversion approach,
637 we optimized the CO₂-to-NO_x ratios for Cairo, Paris, and Beijing in August 2022 based on DQ-1 satellite overpasses and estimated
638 the cities' fossil fuel CO₂ emissions using TROPOMI NO₂ data. The resulting CO₂-to-NO_x ratios ranged from 428–512, 731–742,
639 and 553–640 for Cairo, Paris, and Beijing, respectively, indicating significant day-to-day variability in emission estimates. Cairo
640 exhibited the largest posterior uncertainty, primarily due to high prior uncertainty and transport model errors. Differences in posterior
641 uncertainties across orbits were also closely related to meteorological conditions and the relative position of the satellite tracks to
642 urban plumes. We further compared ffXCO₂ enhancement distributions simulated using the ODIAC inventory. Results for Cairo
643 and Paris were broadly consistent with TROPOMI-based simulations, while notable differences emerged for Beijing. TCCON XCO₂
644 observations were used to interpret these discrepancies. The monthly mean ffXCO₂ enhancement derived from TROPOMI NO₂ data
645 differed from TCCON measurements by less than 1 ppm, whereas the ODIAC-based results deviated by 5.16 ppm. This highlights
646 the need to account for uncertainties arising from inventory allocation and outdated updates when interpreting XCO₂ inversion
647 results. We systematically examined the impact of different prior CO₂-to-NO_x ratio calculation methods on urban ffCO₂ inversions.
648 In our study, methodological differences led to variations of 10.8%–22.8% in prior ratios. Importantly, regardless of the prior ratio

649 or its uncertainty, DQ-1 observations constrained the posterior values to a similar range, substantially reducing discrepancies among
650 different calculation methods.

651 Looking ahead, improving satellite-based city-scale ffCO_2 inversions will require accounting for the spatiotemporal
652 correlations of prior emission errors. Our current framework does not yet incorporate this aspect, which imposes certain limitations
653 on the interpretation and application of the results. Satellite observations are inherently constrained by inversion errors, sampling
654 geometry, and revisit frequency, limiting overpass opportunities. A single prior factor, such as a uniform CO_2 -to- NO_x ratio, cannot
655 fully capture the complex spatiotemporal features of emissions. Incorporating prior error correlations can mitigate uncertainties
656 arising from sparse observations and better resolve temporal and spatial variability in urban emissions. Moreover, the number of
657 satellite tracks required to constrain city emissions depends on the desired emission resolution and uncertainty thresholds relevant
658 for policy applications. Lower temporal resolution may suffice for long-term trend analysis, whereas capturing short-term peaks or
659 episodic emissions necessitates higher observation frequency and precision. This consideration aligns with emerging international
660 approaches emphasizing multi-platform, multi-temporal observations, combining polar-orbiting, geostationary satellites, and
661 ground-based monitoring to achieve multidimensional constraints on urban emissions.

662 Overall, our results demonstrate that coupling high-resolution atmospheric transport simulations with a Bayesian inversion
663 framework allows TROPOMI and DQ-1 multi-source observations to effectively constrain urban ffXCO_2 enhancement signals. The
664 approach captures spatial heterogeneity of emissions, particularly in cities with strong emission intensities and well-defined plume
665 structures, providing a robust basis for quantitative analysis. Furthermore, current methods estimating ffCO_2 from NO_x emissions
666 often lack explicit treatment of CO_2 -to- NO_x ratio uncertainty, which can significantly influence inversion outcomes. Differences
667 among calculation methods for the same region can be as large as 258–304. Notably, our inversion framework substantially reduces
668 CO_2 -to- NO_x ratio uncertainty, providing more stable priors for urban ffCO_2 estimation. Recent studies suggest the need to further
669 optimize CO_2 -to- NO_x emission ratios at regional scales to improve ffCO_2 estimates (Feng et al., 2024). Therefore, we recommend
670 that future NO_x -based ffCO_2 inversion studies adopt observational constraints to refine CO_2 -to- NO_x ratios, minimizing errors arising
671 from prior ratio uncertainties.

672 Appendix

673 A1: ACDL XCO_2 Data Inversion

674 Unlike passive satellite XCO_2 products (e.g., OCO-2/3), the DQ-1 XCO_2 product—hereafter referred to as $\text{XCO}_2^{\text{Lidar}}$ to
675 distinguish it from passive measurements—is derived from the differential absorption between ACDL’s on-band wavelength (strong
676 CO_2 absorption) and off-band wavelength (weak CO_2 absorption). Here, “WF(p)” refers to the lidar signal and integrated weighting
677 function introduced in Section 2.1.1, with “p” representing atmospheric pressure:

678
$$XCO_2^{Lidar} = \frac{2 \cdot \ln \left(\frac{V_{off} \cdot V_{on-0}}{V_{on} \cdot V_{off-0}} \right)}{\int_{p_{surface}}^{p_{toa}} WF(p) dp} \quad (A1)$$

679 Here, V_{on} and V_{off} denote the reflected signal energies at the on-band and off-band wavelengths, respectively, while V_{on-0}
680 and V_{off-0} correspond to the transmitted signal energies. $p_{surface}$ represents the atmospheric pressure at the sub-satellite point
681 of the laser, and p_{toa} denotes the pressure at the top of the atmosphere. The denominator in Equation A1 represents the integrated
682 weighting function ($WF(p)$), which can be expressed according to (Refaat et al., 2016) as:

683
$$WF(p) = \Delta\sigma_{wf}(\lambda_{on}, \lambda_{off}, p) \cdot N_{dry}(p) \quad (A2)$$

684 Here, $\Delta\sigma_{wf}(\lambda_{on}, \lambda_{off}, p)$ represents the differential absorption cross-section of CO₂ between the on-band λ_{on} and off-band λ_{off}
685 wavelengths at pressure p . N_{dry} denotes the number of dry air molecules per unit area within the corresponding pressure layer.

686
687 **Table A1 DQ-1 ACDL operating parameters**

Parameters	Values
Oribit altitude	705km
Lidar footprint diameter	~70m
Horizontal spacing of lidar footprints	~350m
Field of view	<0.2mrad
Telescope diameter	1000nm
Divergence angle after laser beam expansion	<0.1mrad
Repetition frequency	20Hz
Laser pulse width	<50ns
Laser energy	75mJ
Off-line wavelength	1572.085nm
On-line wavelength	1572.024nm

688
689 **A2: Derivation of the Principle of Mass Balance**

690 For satellite column observations of specific species such as NO₂, the mass balance equation can be expressed as follows:

$$\begin{cases} \frac{\partial V_{NO_2}}{\partial t} + \nabla \cdot \vec{F}_{NO_2} = E_{NO_2} - S \\ \vec{F}_{NO} = V_{NO} \vec{u}_{100} \\ S \approx \frac{V_{NO}}{\tau} \end{cases} \quad (A3)$$

Here, V_{NO_2} represents the columnar NO_2 concentration observed by TROPOMI, defined as a scalar function of x and $\nabla =$
 $(\frac{\partial}{\partial x}, \frac{\partial}{\partial y})$ denotes the gradient operator; $\vec{F}_{NO_2} = (F_x, F_y)^T$ is the horizontal flux, with units of $\text{mol} \cdot \text{m}^{-2} \cdot \text{s}^{-1}$, expressed as a vector
 function of x and y and weighted by the wind vector. The 100 m wind field is commonly used to characterize horizontal transport
 within the planetary boundary layer (PBL)(Sun, 2022). τ represents the first-order chemical lifetime of NO_2 in seconds.

By solving the system of equations in Equation A3 and expanding the horizontal flux divergence using vector calculus, we
 obtain the derivation of Equation A4 from Equation A3:

$$\begin{cases} \vec{u}_{100} \cdot (\nabla V_{NO_2}) + V_{NO} (\nabla \cdot \vec{u}_{100}) = \nabla \cdot \vec{F}_{NO} \\ E_{NO_2} = \frac{\partial V_{NO_2}}{\partial t} + \nabla \cdot \vec{F}_{NO} + \frac{V_{NO_2}}{\tau} \end{cases} \quad (A4)$$

Sun et al. 2022, in their first-principles derivation, introduced a "topographic correction term" to replace the wind divergence
 term $V_{NO_2}(\nabla \cdot \vec{u}_{100})$. Beirle et al. 2023 demonstrated that incorporating a topographic correction significantly improves the inversion
 of power-plant NO_x emissions based on the divergence method. Koene et al. 2024 carefully compared these two terms in the
 derivation of the divergence method, showing that they originate from the continuity equations of the source and non-source terms,
 and that numerically, the wind divergence and wind-topography terms are approximately equal in the absence of observational
 errors.

Despite their numerical equivalence in derivation, the accuracy of reanalyzed wind fields is generally lower than that of surface
 elevation data. Therefore, in practical measurements—particularly in complex, fine-scale settings—the wind divergence term alone
 may not provide sufficient constraint. Correcting wind divergence artifacts using topographic gradients is more feasible, especially
 in regions with rugged terrain. Accordingly, we revise Equation A5 using Equation A4 as follows:

$$\frac{V_{NO_2} \vec{u}_{10} \cdot (\nabla z_0)}{H} \approx V_{NO_2} (\nabla \cdot \vec{u}_{100}) \quad (A5)$$

Here, $\frac{V_{NO_2} \vec{u}_{10} \cdot (\nabla z_0)}{H}$ represents the topographic correction term, where the 10 m wind is approximated as the near-surface wind,
 and H denotes the gas scale height in meters. Following previous studies (Beirle et al., 2023; Sun, 2022; Liu et al., 2021), Equation
 A5 is assimilated over both temporal and spatial dimensions. This procedure is concisely represented using the operator $\langle f \rangle$, as
 introduced in the derivations by Liu et al. and Sun et al. Ultimately, this approach allows the derivation of the vertical NO_2 flux on
 a grid-resolved basis.

715 **A3: Atmospheric Model Setting**

716 In this study's application of STILT, hourly outputs from version 4.0 of WRF are used to provide high resolution meteorological
717 fields, with the model grid configured to 32 vertical (eta) layers. The 6-hourly NCEP FNL (Final) global operational analysis data
718 ((ds083.3, $0.25^\circ \times 0.25^\circ$) are used as initial and boundary conditions for meteorological and land surface fields to provide the
719 initial and boundary conditions for WRF runs. The simulations run for 30 hours, but only the 7th to 30th hours of each simulation
720 are used to avoid spin-up effects in the first 6 hours.

721 In this study, we used the STILT model, version 2, to simulate atmospheric transport processes. STILT is configured to release
722 500 particles per receptor each time, with forward dispersion over 24 hours. The particle release heights for STILT are set within
723 the range of 50-1000 m, with releases every 50 m, and 1000-2000 m, with releases every 100 m, the spatial resolution of the STILT
724 simulations is $1 \text{ km} \times 1 \text{ km}$. Generally, as MAXAGL increases from 1 km to 2 km, the urban enhancement increases and then
725 stabilizes.

726 **Table A2 Model version information used in this study**

Model	Version
STILT(Stochastic Time-Inverted Lagrangian Transport)	V2
WRF(Weather Research and Forecasting)	V4.0
X-STILT(X-Stochastic Time-Inverted Lagrangian Transport model)	V1

727

728 **A4: Calculation of NEE XCO₂ enhancement**

729 We performed vertical integration following the method provided by the TCCON team, using the 51 altitude levels listed in
730 the publicly available ak_altitude dataset, which also serve as input heights for the STILT model. In contrast to the XSTILT
731 calculation method used for DQ-1, we applied the integration operator integration_operator_x2019 together with the mean averaging
732 kernel ak_xco2 to the STILT footprints across the 51 levels in order to generate the simulated XSTILT values required for this study.
733 We selected the National Institute for Environmental Studies (Japan) data-driven Upscale Product of Global Gross Primary
734 Production (NEE) as the reference for the overall local NEE during the DQ-1 overpasses. By convolving the NEE inventory with
735 XSTILT, we simulated the XCO₂ enhancement at TCCON sites attributable to NEE.

736 **A5: Calculation of Priori NO_x Emission Uncertainty**

737 The uncertainty of the NO_x inventory derived from the mass balance approach can be estimated using the error propagation
738 law as follows:

$$\varepsilon_{NOx} = \sqrt{\varepsilon_{\alpha}^2 + \varepsilon_{NO2}^2} \quad (A6)$$

where ε_{α} represents the uncertainty in the NO_x/NO_2 ratio, its uncertainty arises from the uncertainties in the input parameters of the chemical model(Liu et al., 2022). And ε_{NO2} denotes the uncertainty in the NO_2 flux field. The latter can be further decomposed as:

$$\varepsilon_{NO2} = \sqrt{\varepsilon_{TROPOMI}^2 + \varepsilon_{Wind}^2 + \varepsilon_{Fit}^2} \quad (A7)$$

Here, $\varepsilon_{TROPOMI}$ is the uncertainty of the NO_2 column concentration, ε_{Wind} represents the uncertainty associated with the wind field, and ε_{Fit} accounts for the uncertainty in the fitted vertical scale height and chemical lifetime. The uncertainty of NO_2 arises from multiple factors, including spectral fitting, stratospheric correction, AMF, clouds, vertical profiles, and surface albedo(Boersma et al., 2018; Verhoelst et al., 2021; Van Geffen et al., 2022; Boersma et al., 2004; Martin et al., 2002; Lu et al., 2025). In this study, we use the ratio of the standard deviation to the mean of the column concentration within the study area as a proxy for the TROPOMI observational noise, integrated over the time series. It should be noted that this proxy is calculated based on the oversampled gridded data (also referred to as Level-3) rather than the original Level-2 orbit data. In this study, we do not account for errors introduced during the oversampling of TROPOMI L2 data to the grid(Glissenaar et al., 2025). With appropriate gridding, the uncertainty in polluted areas can be reduced by approximately 20% compared with the original orbits(Sun et al., 2018a). Wind field uncertainty is quantified through 10^4 Monte Carlo perturbations of wind speed and direction, with the propagated standard deviation representing the flux variability. The fitting uncertainty is obtained by performing 10^4 Monte Carlo draws of the grids involved in the fit, generating ensembles of scale heights and chemical lifetimes, with the final fitting error defined as the root mean square of the standard deviations of these ensembles.

Using the method described above, we quantified the overall uncertainty of NO_x prior emissions for three cities, as well as the contributions from individual components, with the detailed results summarized in Table A3. It should be noted that the uncertainties reported here represent aggregated values for the entire urban area, rather than detailed uncertainties for individual grid cells.

Based on the uncertainty calculations, the total uncertainty follows the order Beijing (23.79%) > Paris (18.15%) > Cairo (14.31%). A closer look at the contributions of individual components reveals that NO_2 column concentrations and the wind field are the dominant sources, together accounting for more than 66.7% of the total uncertainty. This is attributable to the nature of data-driven dispersion models, in which uncertainties in wind and concentration directly govern the overall uncertainty(Sun, 2022). The nonlinear gradient operations in dispersion models (e.g., second-order difference operators) can amplify white noise in the original concentration field, while in existing emission quantification models, wind fields are considered a major source of uncertainty due to sparse monitoring sites and model errors(Huang et al., 2025).

Among the three cities, NO_2 column inversion uncertainty is highest in Beijing. Unlike Cairo, where high surface reflectivity eases retrievals, Beijing is located in the highly polluted North China Plain with elevated AOD, which increases the difficulty of

769 passive column inversion. In addition, Beijing’s complex terrain contributes to the highest wind field uncertainty (~17%) among the
 770 three cities. The NO_x/NO₂ uncertainty is roughly similar across the three cities, consistent with previous studies using NU-WRF
 771 (~1.4 ± 0.1). In contrast, the uncertainty associated with first-order chemical lifetime and vertical scale height is the lowest among
 772 all components (~1%). This is different from earlier studies (~15%)(Liu et al., 2022) and reflects the benefit of the data-driven fitting
 773 approach proposed by Sun et al. (see main text). Since no new assumptions were introduced in the current study, this uncertainty
 774 arises solely from the linear fitting model.

775 **Table A3 The overall uncertainty of NO_x emissions and the uncertainties of individual components were derived using the dispersion**
 776 **model.**

	NO _x /NO ₂ uncertainty(%)	NO ₂ uncertainty(%)	Wind uncertainty(%)	Fitted uncertainty(%)	Total uncertainty(%)
Beijing	6.51	15.49	16.76	1.67	23.79
Cairo	4.79	11.64	6.76	0.78	14.31
Paris	5.02	13.67	10.76	1.21	18.15

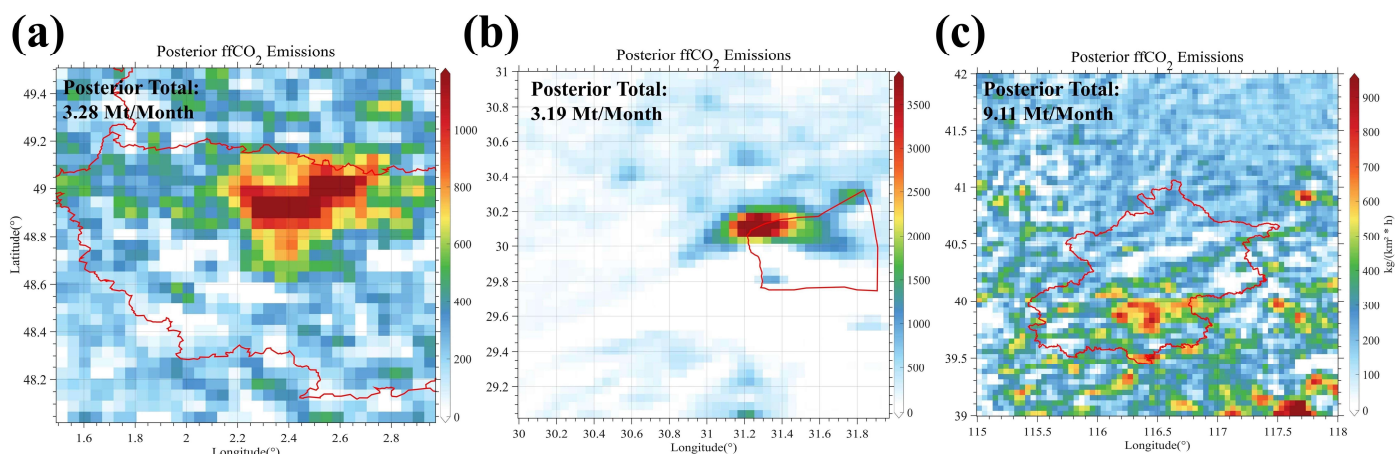
777

778 **A6: Optimization results of the CO₂-to-NO_x ratio obtained using different calculation methods**

779 **Table A4 Inversion results of CO₂-to-NO_x ratios calculated using different methods**

Method	City	Date	Prior CO ₂ - to- NO _x ratio (λ)	CO ₂ -to- NO _x ratio uncertainty (%)	NO _x emission uncertainty (%)	Prior uncertainty (%)	Posterior CO ₂ - to-NO _x ratio (λ)	Posterior uncertainty (%)
1	Beijing	2022/8/9	694	15	23.79	28.12	640	14.08
	Beijing	2022/8/16	694	15	23.79	28.12	553	16.24
	Cairo	2022/8/2	470	37.99	14.31	40.60	428	15.09
	Cairo	2022/8/19	470	37.99	14.31	40.60	512	18.86
	Paris	2022/8/7	601	24.04	18.15	30.12	731	14.72
	Paris	2022/8/21	601	24.04	18.15	30.12	742	18.67
2	Beijing	2022/8/9	632	28.28	23.79	36.96	624	16.08

	Beijing	2022/8/16	632	28.28	23.79	36.96	521	18.8
	Cairo	2022/8/2	302	56.56	14.31	58.34	402	23.21
	Cairo	2022/8/19	302	56.56	14.31	58.34	497	22.14
	Paris	2022/8/7	412	35.35	18.15	39.74	698	19.65
	Paris	2022/8/21	412	35.35	18.15	39.74	649	26.14
3	Beijing	2022/8/9	732	20.02	23.79	31.09	653	17.65
	Beijing	2022/8/16	732	20.02	23.79	31.09	545	21.32
	Cairo	2022/8/2	450	45.81	14.31	47.99	412	18.74
	Cairo	2022/8/19	450	45.08	14.31	47.99	503	20.41
	Paris	2022/8/7	472	24.83	18.15	30.75	697	16.84
	Paris	2022/8/21	472	24.83	18.15	30.75	701	19.65
4	Beijing	2022/8/9	522	26.12	23.79	35.33	594	18.44
	Beijing	2022/8/16	522	26.12	23.79	35.33	491	15.69
5	Beijing	2022/8/9	654	18.72	23.79	30.27	630	14.99
	Beijing	2022/8/16	654	18.72	23.79	30.27	536	20.52
	Cairo	2022/8/2	420	41.32	14.31	43.73	421	16.79
	Cairo	2022/8/19	420	41.32	14.31	43.73	532	20.93
	Paris	2022/8/7	539	28.31	18.15	33.63	720	16.55
	Paris	2022/8/21	539	28.31	18.15	33.63	718	20.83
6	Beijing	2022/8/9	610	28.28	23.79	36.96	619	16.55
	Beijing	2022/8/16	610	28.28	23.79	36.96	509	16.76
	Cairo	2022/8/2	264	56.56	14.31	58.34	403	19.47
	Cairo	2022/8/19	264	56.56	14.31	58.34	467	28.12
	Paris	2022/8/7	492	35.35	18.15	39.74	687	23.34
	Paris	2022/8/21	492	35.35	18.15	39.74	712	23.14



781
 782 **Figure A1: Posterior fossil fuel carbon dioxide emissions for each city. The red lines outline city boundaries, while the colored shading**
 783 **indicates carbon dioxide emission distribution.**

784 **Declaration of Competing Interest**

785 The authors declare that they have no known competing financial interests or personal relationships that could have appeared
 786 to influence the work reported in this paper.

787 **Acknowledgments**

788 The authors thank all the financial support for this research. This research was supported by the National Key R&D Program
 789 of China (Grant No. 2024YFB3910203), National Natural Science Foundation of China(Grant No. 42475144), the Fundamental
 790 Research Funds for the Central Universities(2042025kf0036) and Beijing Natural Science Foundation (Grant No. L211045).

791 **Author contributions**

792 The experiment design was made by GH and JY. The data collection was done by JY, YH, HL, GH. JY completed the design
 793 of the overall WRF-STILT model workflow, data collection, and result analysis. The data analysis was done by HZ, YZ, TS. WG
 794 and SL provide funding. The paper was written by JY and GH. All authors have reviewed, commented on, and approved the paper.

795 **Reference**

796 Agency, I. E.: World energy outlook, OECD/IEA Paris2009.
 797 Andres, R. J., Boden, T. A., Bréon, F.-M., Ciais, P., Davis, S., Erickson, D., Gregg, J. S., Jacobson, A., Marland, G., and Miller, J.:
 798 A synthesis of carbon dioxide emissions from fossil-fuel combustion, Biogeosciences, 9, 1845-1871, 2012.

799 Ayazpour, Z., Sun, K., Zhang, R., and Shen, H.: Evaluation of the Directional Derivative Approach for Timely and Accurate Satellite-
800 Based Emission Estimation Using Chemical Transport Model Simulation of Nitrogen Oxides, *Journal of Geophysical Research: Atmospheres*, 130, e2024JD042817, <https://doi.org/10.1029/2024JD042817>, 2025.

802 Beirle, S., Borger, C., Jost, A., and Wagner, T.: Improved catalog of NO_x point source emissions (version 2), *Earth system science data discussions*, 2023, 1-37, 2023.

804 Berezin, E., Kononov, I., Ciais, P., Richter, A., Tao, S., Janssens-Maenhout, G., Beekmann, M., and Schulze, E.-D.: Multiannual
805 changes of CO₂ emissions in China: indirect estimates derived from satellite measurements of tropospheric NO₂ columns, *Atmospheric Chemistry and Physics*, 13, 9415-9438, 2013.

807 Boersma, K. F., Eskes, H. J., and Brinksma, E. J.: Error analysis for tropospheric NO₂ retrieval from space, *Journal of Geophysical Research: Atmospheres*, 109, <https://doi.org/10.1029/2003JD003962>, 2004.

809 Boersma, K. F., Eskes, H. J., Richter, A., De Smedt, I., Lorente, A., Beirle, S., van Geffen, J. H. G. M., Zara, M., Peters, E., Van
810 Roozendaal, M., Wagner, T., Maasakkers, J. D., van der A, R. J., Nightingale, J., De Rudder, A., Irie, H., Pinardi, G., Lambert,
811 J. C., and Compennolle, S. C.: Improving algorithms and uncertainty estimates for satellite NO₂ retrievals: results from the
812 quality assurance for the essential climate variables (QA4ECV) project, *Atmos. Meas. Tech.*, 11, 6651-6678, 10.5194/amt-11-
813 6651-2018, 2018.

814 Brenninkmeijer, C. A. and Cai, D. S.: Earth System Chemistry integrated Modelling (ESCiMo) with the Modular Earth Submodel
815 System (MESSy) version 2.51, *Geoscientific Model Development*, 9, 1153, 2016.

816 Che, K., Lauvaux, T., Taquet, N., Stremme, W., Xu, Y., Alberti, C., Lopez, M., García-Reynoso, A., Ciais, P., and Liu, Y.: CO₂
817 emissions estimate from Mexico City using ground-and space-based remote sensing, *Journal of Geophysical Research: Atmospheres*, 129, e2024JD041297, 2024.

819 Che, K., Cai, Z., Liu, Y., Wu, L., Yang, D., Chen, Y., Meng, X., Zhou, M., Wang, J., Yao, L., and Wang, P.: Lagrangian inversion of
820 anthropogenic CO₂ emissions from Beijing using differential column measurements, *Environmental Research Letters*, 17,
821 075001, 10.1088/1748-9326/ac7477, 2022.

822 Cheng, C., Liu, D., Wang, S., Zhang, X., Zhang, L., Chen, W., Liu, J., Wan, X., Chen, W., and Chen, X.: Estimating strong point
823 CO₂ emissions by combining spaceborne IPDA lidar and HSRL, *Remote Sensing of Environment*, 328, 114898, 2025.

824 Crippa, M., Guizzardi, D., Muntean, M., Schaaf, E., Dentener, F., Van Aardenne, J. A., Monni, S., Doering, U., Olivier, J. G., and
825 Pagliari, V.: Gridded emissions of air pollutants for the period 1970–2012 within EDGAR v4. 3.2, *Earth Syst. Sci. Data*, 10,
826 1987-2013, 2018.

827 Dai, G., Wu, S., Long, W., Liu, J., Xie, Y., Sun, K., Meng, F., Song, X., Huang, Z., and Chen, W.: Aerosol and cloud data processing
828 and optical property retrieval algorithms for the spaceborne ACDC/DQ-1, *Atmospheric Measurement Techniques*, 17, 1879-
829 1890, 2024.

830 Danielson, J. J. and Gesch, D. B.: Global multi-resolution terrain elevation data 2010 (GMTED2010), *US Geological Survey* 2331-
831 1258, 2011.

832 Dickerson, R. R., Stedman, D. H., and Delany, A. C.: Direct measurements of ozone and nitrogen dioxide photolysis rates in the
833 troposphere, *Journal of Geophysical Research: Oceans*, 87, 4933-4946, 1982.

834 Eldering, A., Wennberg, P., Crisp, D., Schimel, D., Gunson, M., Chatterjee, A., Liu, J., Schwandner, F., Sun, Y., and O'dell, C.: The
835 Orbiting Carbon Observatory-2 early science investigations of regional carbon dioxide fluxes, *Science*, 358, eaam5745, 2017.

836 Eskes, H., van Geffen, J., Sneep, M., Veeffkind, P., Niemeijer, S., and Zehner, C.: S5P Nitrogen Dioxide v02. 03.01 intermediate
837 reprocessing on the S5P-PAL system: Readme file, *ESA*, 12,

838 Feng, S., Jiang, F., Wang, H., Liu, Y., He, W., Wang, H., Shen, Y., Zhang, L., Jia, M., and Ju, W.: China's fossil fuel CO₂ emissions
839 estimated using surface observations of coemitted NO₂, *Environmental Science & Technology*, 58, 8299-8312, 2024.

840 Gately, C. K. and Hutyra, L. R.: Large uncertainties in urban-scale carbon emissions, *Journal of Geophysical Research: Atmospheres*,
841 122, 11,242-211,260, 2017.

842 Glissenaar, I., Boersma, K. F., Angloul, I., Rijsdijk, P., Verhoelst, T., Compennolle, S., Pinardi, G., Lambert, J.-C., Van Roozendaal,
843 M., and Eskes, H.: TROPOMI Level 3 tropospheric NO₂ dataset with advanced uncertainty analysis from the ESA CCI+ ECV
844 precursor project, *Earth System Science Data*, 17, 4627-4650, 2025.

845 Hakkarainen, J., Ialongo, I., and Tamminen, J.: Direct space-based observations of anthropogenic CO₂ emission areas from OCO-
846 2, *Geophysical Research Letters*, 43, 11,400-411,406, 2016.

847 Han, G., Ma, X., Liang, A., Zhang, T., Zhao, Y., Zhang, M., and Gong, W.: Performance evaluation for China's planned CO₂-IPDA,
848 *Remote Sensing*, 9, 768, 2017.

849 Han, G., Xu, H., Gong, W., Liu, J., Du, J., Ma, X., and Liang, A.: Feasibility Study on Measuring Atmospheric CO₂ in Urban Areas
850 Using Spaceborne CO₂-IPDA LIDAR, *Remote Sensing*, 10, 985, 2018.

851 Han, G., Huang, Y., Shi, T., Zhang, H., Li, S., Zhang, H., Chen, W., Liu, J., and Gong, W.: Quantifying CO₂ emissions of power
852 plants with Aerosols and Carbon Dioxide Lidar onboard DQ-1, *Remote Sensing of Environment*, 313, 114368,
853 <https://doi.org/10.1016/j.rse.2024.114368>, 2024.

854 Han, G., Zhang, H., Huang, Y., Chen, W., Mao, H., Zhang, X., Ma, X., Li, S., Zhang, H., and Liu, J.: First global XCO₂ observations
855 fromspaceborne lidar: methodology and initial result, *Remote Sensing of Environment*, 330, 114954, 2025.

856 Hersbach, H., Bell, B., Berrisford, P., Biavati, G., Horányi, A., Muñoz Sabater, J., Nicolas, J., Peubey, C., Radu, R., and Rozum, I.:
857 ERA5 hourly data on single levels from 1940 to present, Copernicus climate change service (c3s) climate data store (cds), 10,
858 2023.

859 Huang, T., Zhu, X., Zhong, Q., Yun, X., Meng, W., Li, B., Ma, J., Zeng, E. Y., and Tao, S.: Spatial and temporal trends in global
860 emissions of nitrogen oxides from 1960 to 2014, *Environmental science & technology*, 51, 7992-8000, 2017.

861 Huang, Y., Han, G., Shi, T., Li, S., Mao, H., Nie, Y., and Gong, W.: Fi-scape: a divergence theorem based emission quantification
862 model for air/space-borne imaging spectrometer derived xch₄ observations, *IEEE Journal of Selected Topics in Applied Earth
863 Observations and Remote Sensing*, 2024.

864 Huang, Y., Han, G., Yi, J., Shi, T., Zhang, Y., Luo, H., Mao, H., Li, S., Mao, F., and Gong, W.: Rapid methane flux estimation
865 combining MethaneSAT and Sentinel-5P observations: A case study of Turkmenistan, *Geophysical Research Letters*, 52,
866 e2025GL119369, 2025.

867 Kiemle, C., Ehret, G., Amediek, A., Fix, A., Quatrevalet, M., and Wirth, M.: Potential of Spaceborne Lidar Measurements of Carbon
868 Dioxide and Methane Emissions from Strong Point Sources, *Remote Sensing*, 9, 1137, 2017.

869 Kiemle, C., Quatrevalet, M., Ehret, G., Amediek, A., Fix, A., and Wirth, M.: Sensitivity studies for a space-based methane lidar
870 mission, *Atmospheric Measurement Techniques*, 4, 2195-2211, 2011.

871 Koene, E. F. M., Brunner, D., and Kuhlmann, G.: On the theory of the divergence method for quantifying source emissions from
872 satellite observations, *Journal of Geophysical Research: Atmospheres*, 129, e2023JD039904, 2024.

873 Köhler, P., Guanter, L., Kobayashi, H., Walther, S., and Yang, W.: Assessing the potential of sun-induced fluorescence and the
874 canopy scattering coefficient to track large-scale vegetation dynamics in Amazon forests, *Remote Sensing of Environment*,
875 204, 769-785, <https://doi.org/10.1016/j.rse.2017.09.025>, 2018.

876 Konovalov, I. B., Berezin, E. V., Ciais, P., Broquet, G., Zhuravlev, R. V., and Janssens-Maenhout, G.: Estimation of fossil-fuel CO
877 2 emissions using satellite measurements of " proxy" species, *Atmospheric Chemistry and Physics*, 16, 13509-13540, 2016.

878 Le Quéré, C., Andrew, R. M., Friedlingstein, P., Sitch, S., Hauck, J., Pongratz, J., Pickers, P. A., Korsbakken, J. I., Peters, G. P., and
879 Canadell, J. G.: Global carbon budget 2018, *Earth System Science Data*, 10, 2141-2194, 2018.

880 Lin, J. and Gerbig, C.: Accounting for the effect of transport errors on tracer inversions, *Geophysical Research Letters*, 32, 2005.

881 Liu, F., Tao, Z., Beirle, S., Joiner, J., Yoshida, Y., Smith, S. J., Knowland, K. E., and Wagner, T.: A new method for inferring city
882 emissions and lifetimes of nitrogen oxides from high-resolution nitrogen dioxide observations: a model study, *Atmospheric
883 Chemistry and Physics*, 22, 1333-1349, 2022.

884 Liu, F., Duncan, B. N., Krotkov, N. A., Lamsal, L. N., Beirle, S., Griffin, D., McLinden, C. A., Goldberg, D. L., and Lu, Z.: A
885 methodology to constrain carbon dioxide emissions from coal-fired power plants using satellite observations of co-emitted
886 nitrogen dioxide, *Atmospheric Chemistry and Physics*, 20, 99-116, 2020.

887 Liu, M., Van Der A, R., Van Weele, M., Eskes, H., Lu, X., Veeffkind, P., De Laat, J., Kong, H., Wang, J., and Sun, J.: A new divergence
888 method to quantify methane emissions using observations of Sentinel-5P TROPOMI, *Geophysical Research Letters*, 48,
889 e2021GL094151, 2021.

890 Lu, L., Cohen, J. B., Qin, K., Tiwari, P., Hu, W., Gao, H., and Zheng, B.: New Perspective on Using Observational Uncertainty to

891 Improve Reliability of NO_x Emissions Over Northern China, *IEEE Transactions on Geoscience and Remote Sensing*, 63, 1-
892 15, 10.1109/TGRS.2025.3620116, 2025.

893 Martin, R. V., Chance, K., Jacob, D. J., Kurosu, T. P., Spurr, R. J. D., Bucsela, E., Gleason, J. F., Palmer, P. I., Bey, I., Fiore, A. M.,
894 Li, Q., Yantosca, R. M., and Koelemeijer, R. B. A.: An improved retrieval of tropospheric nitrogen dioxide from GOME,
895 *Journal of Geophysical Research: Atmospheres*, 107, ACH 9-1-ACH 9-21, <https://doi.org/10.1029/2001JD001027>, 2002.

896 Miller, J. B., Tans, P. P., and Gloor, M.: Steps for success of OCO-2, *Nature Geoscience*, 7, 691-691, 2014.

897 Oda, T. and Maksyutov, S.: ODIAC Fossil Fuel CO₂ Emissions Dataset (version: ODIAC2020b), Center for Global Environmental
898 Research, National Institute for Environmental Studies [data set], <https://doi.org/10.17595/20170411.001>, 2015.

899 Oda, T., Bun, R., Kinakh, V., Topylko, P., Halushchak, M., Marland, G., Lauvaux, T., Jonas, M., Maksyutov, S., and Nahorski, Z.:
900 Errors and uncertainties in a gridded carbon dioxide emissions inventory, *Mitigation and Adaptation Strategies for Global
901 Change*, 24, 1007-1050, 2019.

902 Qin, K., Lu, L., Liu, J., He, Q., Shi, J., Deng, W., Wang, S., and Cohen, J. B.: Model-free daily inversion of NO_x emissions using
903 TROPOMI (MCMFE-NO_x) and its uncertainty: Declining regulated emissions and growth of new sources, *Remote Sensing
904 of Environment*, 295, 113720, 2023.

905 Refaat, T. F., Singh, U. N., Yu, J., Petros, M., Remus, R., and Ismail, S.: Double-pulse 2- μ m integrated path differential absorption
906 lidar airborne validation for atmospheric carbon dioxide measurement, *Applied Optics*, 55, 4232-4246, 2016.

907 Reuter, M., Buchwitz, M., Schneising, O., Krautwurst, S., O'Dell, C. W., Richter, A., Bovensmann, H., and Burrows, J. P.: Towards
908 monitoring localized CO₂ emissions from space: co-located regional CO₂ and NO₂ enhancements observed by the OCO-2
909 and S5P satellites, *Atmospheric Chemistry and Physics*, 19, 9371-9383, 2019.

910 Rey-Pommier, A., Chevallier, F., Ciais, P., Christoudias, T., Kushta, J., Georgiou, G., Violaris, A., Dubart, F., and Sciare, J.: Mapping
911 NO_x emissions in Cyprus using TROPOMI observations: evaluation of the flux-divergence scheme using multiple parameter
912 sets, *Environmental Science and Pollution Research*, 32, 1932-1951, 2025.

913 Schwandner, F. M., Gunson, M. R., Miller, C. E., Carn, S. A., Eldering, A., Krings, T., Verhulst, K. R., Schimel, D. S., Nguyen, H.
914 M., and Crisp, D.: Spaceborne detection of localized carbon dioxide sources, *Science*, 358, eaam5782, 2017.

915 Sheng, M., Hou, Y., Song, H., Ye, X., Lei, L., Ma, P., and Zeng, Z.-C.: Estimating anthropogenic CO₂ emissions from China's
916 Yangtze River Delta using OCO-2 observations and WRF-Chem simulations, *Remote Sensing of Environment*, 316, 114515,
917 2025.

918 Sun, K.: Derivation of emissions from satellite-observed column amounts and its application to TROPOMI NO₂ and CO
919 observations, *Geophysical Research Letters*, 49, e2022GL101102, 2022.

920 Sun, K., Li, L., Jagini, S., and Li, D.: A Satellite Data-Driven Framework to Rapidly Quantify Air Basin-Scale NO_x Emission and
921 Its Application to the Po Valley during the COVID-19 Pandemic, *Atmospheric Chemistry and Physics Discussions*, 2021, 1-
922 29, 2021.

923 Sun, K., Zhu, L., Cady-Pereira, K., Chan Miller, C., Chance, K., Clarisse, L., Coheur, P.-F., González Abad, G., Huang, G., and Liu,
924 X.: A physics-based approach to oversample multi-satellite, multispecies observations to a common grid, *Atmospheric
925 Measurement Techniques*, 11, 6679-6701, 2018a.

926 Sun, Y., Frankenberg, C., Jung, M., Joiner, J., Guanter, L., Köhler, P., and Magney, T.: Overview of Solar-Induced chlorophyll
927 Fluorescence (SIF) from the Orbiting Carbon Observatory-2: Retrieval, cross-mission comparison, and global monitoring for
928 GPP, *Remote Sensing of Environment*, 209, 808-823, <https://doi.org/10.1016/j.rse.2018.02.016>, 2018b.

929 Team, M.: The Multi-resolution Emission Inventory Model for Climate and Air Pollution Research, MEIC Model [data set], 2012.

930 van Geffen, J., Eskes, H., Compornolle, S., Pinardi, G., Verhoelst, T., Lambert, J. C., Sneep, M., ter Linden, M., Ludewig, A.,
931 Boersma, K. F., and Veefkind, J. P.: Sentinel-5P TROPOMI NO₂ retrieval: impact of version v2.2 improvements and
932 comparisons with OMI and ground-based data, *Atmos. Meas. Tech.*, 15, 2037-2060, 10.5194/amt-15-2037-2022, 2022.

933 Veefkind, J. P., Aben, I., McMullan, K., Förster, H., De Vries, J., Otter, G., Claas, J., Eskes, H., De Haan, J., and Kleipool, Q.:
934 TROPOMI on the ESA Sentinel-5 Precursor: A GMES mission for global observations of the atmospheric composition for
935 climate, air quality and ozone layer applications, *Remote sensing of environment*, 120, 70-83, 2012.

936 Verhoelst, T., Compornolle, S., Pinardi, G., Lambert, J. C., Eskes, H. J., Eichmann, K. U., Fjæraa, A. M., Granville, J., Niemeijer,

937 S., Cede, A., Tiefengraber, M., Hendrick, F., Pazmiño, A., Bais, A., Bazureau, A., Boersma, K. F., Bognar, K., Dehn, A., Donner,
938 S., Elokhov, A., Gebetsberger, M., Goutail, F., Grutter de la Mora, M., Gruzdev, A., Gratsea, M., Hansen, G. H., Irie, H., Jepsen,
939 N., Kanaya, Y., Karagkiozidis, D., Kivi, R., Kreher, K., Levelt, P. F., Liu, C., Müller, M., Navarro Comas, M., PETERS, A. J. M.,
940 Pommereau, J. P., Portafaix, T., Prados-Roman, C., Puenteadura, O., Querel, R., Remmers, J., Richter, A., Rimmer, J., Rivera
941 Cárdenas, C., Saavedra de Miguel, L., Sinyakov, V. P., Stremme, W., Strong, K., Van Roozendaal, M., Veefkind, J. P., Wagner,
942 T., Wittrock, F., Yela González, M., and Zehner, C.: Ground-based validation of the Copernicus Sentinel-5P TROPOMI NO₂
943 measurements with the NDACC ZSL-DOAS, MAX-DOAS and Pandonia global networks, *Atmos. Meas. Tech.*, 14, 481-510,
944 10.5194/amt-14-481-2021, 2021.

945 Wang, J., Kawa, S., Eluszkiewicz, J., Baker, D., Mountain, M., Henderson, J., Nehr Korn, T., and Zaccheo, T.: A regional CO₂
946 observing system simulation experiment for the ASCENDS satellite mission, *Atmospheric Chemistry and Physics*, 14, 12897-
947 12914, 2014.

948 Wang, R., Tao, S., Ciais, P., Shen, H., Huang, Y., Chen, H., Shen, G., Wang, B., Li, W., and Zhang, Y.: High-resolution mapping of
949 combustion processes and implications for CO₂ emissions, *Atmospheric Chemistry and Physics*, 13, 5189-5203, 2013.

950 Wei, C.: Historical trend and drivers of China's CO₂ emissions from 2000 to 2020, *Environment, development and sustainability*,
951 26, 2225-2244, 2024.

952 Wu, D., Lin, J. C., Fasoli, B., Oda, T., Ye, X., Lauvaux, T., Yang, E. G., and Kort, E. A.: A Lagrangian approach towards extracting
953 signals of urban CO₂ emissions from satellite observations of atmospheric column CO₂ (XCO₂): X-Stochastic Time-Inverted
954 Lagrangian Transport model ("X-STILT v1"), *Geoscientific Model Development*, 11, 4843-4871, 2018.

955 Xu, J., Guan, Y., Oldfield, J., Guan, D., and Shan, Y.: China carbon emission accounts 2020-2021, *Applied Energy*, 360, 122837,
956 2024.

957 Xu, T., Zhang, C., and Liu, C.: Enhanced quantification of global carbon emitters using collocated OCO-3 CO₂ and NO₂
958 observations from twin polar-orbiting satellites, *Geophysical Research Letters*, 52, e2025GL116877, 2025.

959 Yang, E. G., Kort, E. A., Ott, L. E., Oda, T., and Lin, J. C.: Using space-based CO₂ and NO₂ observations to estimate urban CO₂
960 emissions, *Journal of Geophysical Research: Atmospheres*, 128, e2022JD037736, 2023.

961 Ye, X., Lauvaux, T., Kort, E. A., Oda, T., Feng, S., Lin, J. C., Yang, E. G., and Wu, D.: Constraining fossil fuel CO₂ emissions from
962 urban area using OCO-2 observations of total column CO₂, *Journal of Geophysical Research: Atmospheres*, 125,
963 e2019JD030528, 2020.

964 Yi, J., Huang, Y., Pei, Z., and Han, G.: Urban area observing system (UAOS) simulation experiment using DQ-1 total column
965 concentration observations, *EGUsphere*, 2024, 1-40, 2024.

966 Yi, J., Huang, Y., Pei, Z., and Han, G.: Urban Area Observing System (UAOS) simulation experiment using DQ-1 total column
967 concentration observations, *Atmospheric Chemistry and Physics*, 25, 13687-13710, 2025.

968 Zhang, Q., Boersma, K. F., Zhao, B., Eskes, H., Chen, C., Zheng, H., and Zhang, X.: Quantifying daily NO_x and CO₂ emissions
969 from Wuhan using satellite observations from TROPOMI and OCO-2, *Atmospheric Chemistry and Physics Discussions*, 2022,
970 1-18, 2022.

971 Zhang, Q., Streets, D. G., Carmichael, G. R., He, K., Huo, H., Kannari, A., Klimont, Z., Park, I., Reddy, S., and Fu, J.: Asian
972 emissions in 2006 for the NASA INTEX-B mission, *Atmospheric Chemistry and Physics*, 9, 5131-5153, 2009.

973 Zhang, X., Yang, H., Bu, L., Fan, Z., Xiao, W., Chen, B., Zhang, L., Liu, S., Wang, Z., and Liu, J.: Estimation of diurnal emissions
974 of CO₂ from thermal power plants using spaceborne integrated path differential absorption (IPDA) lidar, *Atmospheric
975 Chemistry and Physics*, 25, 6725-6740, 2025.

976 Zheng, B., Geng, G., Ciais, P., Davis, S. J., Martin, R. V., Meng, J., Wu, N., Chevallier, F., Broquet, G., and Boersma, F.: Satellite-
977 based estimates of decline and rebound in China's CO₂ emissions during COVID-19 pandemic, *Science advances*, 6, eabd4998,
978 2020.

979